Deposition of sulfate aerosols with positive Δ33S in the Neoarchean

Guillaume Paris, Woodward W Fischer, Jena E Johnson, Samuel M Webb, Theodore M Present, Alex L Sessions, Jess F Adkins

Journal Pre-proofs

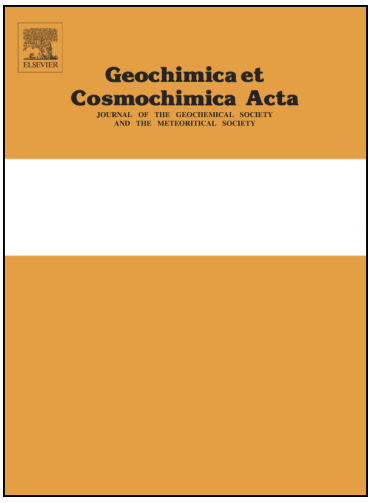

Deposition of sulfate aerosols with positive $\Delta^{33}S$ in the Neoarchean

Guillaume Paris, Woodward W. Fischer, Jena E. Johnson, Samuel M. Webb, Theodore M. Present, Alex L. Sessions, Jess F. Adkins

PII: S0016-7037(20)30405-1
DOI: https://doi.org/10.1016/j.gca.2020.06.028
Reference: GCA 11820

To appear in: *Geochimica et Cosmochimica Acta*

Received Date: 21 February 2020
Revised Date: 23 June 2020
Accepted Date: 24 June 2020

Please cite this article as: Paris, G., Fischer, W.W., Johnson, J.E., Webb, S.M., Present, T.M., Sessions, A.L., Adkins, J.F., Deposition of sulfate aerosols with positive $\Delta^{33}S$ in the Neoarchean, *Geochimica et Cosmochimica Acta* (2020), doi: https://doi.org/10.1016/j.gca.2020.06.028

Deposition of sulfate aerosols with positive $\Delta^{33}S$ in the Neoarchean

Guillaume Paris[1], Woodward W. Fischer[2], Jena E. Johnson[3], Samuel M. Webb[4], Theodore M. Present[2], Alex L. Sessions[2], Jess F. Adkins[2]

[1] CRPG, 15 rue Notre-Dame des Pauvres, UMR 7358 Université de Lorraine-CNRS 54000 Nancy, France

[2] Division of Geological and Planetary Sciences, California Institute of Technology, Pasadena, CA 91125, USA

[3] Department of Earth and Environmental Sciences, University of Michigan, Ann Arbor MI 48103, USA

[4] Stanford Synchrotron Radiation Lightsource, Stanford University, Menlo Park, CA 94025, USA

Corresponding author: Guillaume Paris, guillaume.paris@univ-lorraine.fr

Abstract

Anomalous sulfur isotope compositions present in Archean rocks have been intensely scrutinized over the last 20 years because they record key aspects of Earth's atmospheric composition prior to the appearance of free molecular oxygen *ca.* 2.3 billion years ago. These isotopic compositions can be described as mass anomalous fractionations (MAF) and are produced in the atmosphere as UV light interacts with SO_2 molecules. Most interpretations suggest that atmospheric processes generate a reduced S-phase with a positive (^{33}S-enriched) MAF signature, as measured in pyrites, and an oxidized S-phase with a negative anomaly, as measured in bedded barite deposits. However, recent data for carbonate-associated sulfate (CAS) — a direct proxy for the isotopic composition of sulfur from seawater sulfate — in Neoarchean rocks showed no such negative values, but rather the opposite. To understand if the positive MAF anomalies we measured in Neoarchean CAS reflect secondary processes (diagenetic, metamorphic, handling) instead of original signals of Archean seawater sulfate, we collected additional sample suites with various degrees of preservation and metamorphic alteration across the Campbellrand-Malmani platform in South Africa. Results illustrate that within this comprehensive suite, less-altered samples all

contain positive MAF values while secondary processes tend to either remove CAS from the sample and/or decrease the ^{33}S-enrichment. This positive MAF signal in sulfate is therefore reasonably interpreted as a primary depositional origin, and implies that the assumption that sulfate always carries a negative MAF anomaly throughout the Archean rock record needs to be reconsidered. Our CAS observations suggest that future experiments and calculations should also consider atmospheric and/or sulfur cycling processes that can produce oxidized sulfur with a positive MAF signature.

1. Introduction

The evolution of Earth's atmosphere through geological time is a long-standing problem in the Earth Sciences. During Archean time (4.0 to 2.5 Ga), the Earth was characterized by a lack of oxygen in the atmosphere and oceans (Holland, 1984; Fischer et al., 2016). Despite a lower intensity of solar irradiation, liquid water was sustained at Earth's surface, suggesting a significantly higher greenhouse gas content in the Archean atmosphere compared to today's (Sagan and Mullen, 1972; Kasting, 1989). The major greenhouse gas is thought to have been carbon dioxide (CO_2) possibly together with much higher methane (CH_4) concentrations, with contributions from carbonyl sulfide (COS), ammonia (NH_3) or other greenhouse gases (e.g. Sagan and Chyba, 1997; Zahnle et al., 2006; Domagal-Goldman et al., 2008; Thomazo et al., 2009; Ueno et al., 2009). It is therefore of great interest to characterize not only the evolution of O_2, but also the different gases that helped sustain liquid water on the early Earth. Because they are thought to have originated from reactions in the atmosphere, anomalous multiple sulfur isotope ratios (Farquhar et al., 2000) offer the opportunity of constraining multiple gas components at once (e.g. Endo et al., 2016).

Unusual sulfur isotope compositions have been observed in Archean sedimentary rocks until their disappearance from the rock record in early Proterozoic time associated with the Great Oxygenation Event (Farquhar et al., 2000; Ono et al., 2003; Guo et al., 2009; Johnston, 2011; Luo et al., 2016; Philippot et al., 2018). Most processes on Earth separate sulfur isotopes in proportion to their relative mass difference, generating "mass-dependent fractionations" (MDF), so called because they follow a canonical equilibrium fractionation law (Hulston and Thode, 1965; Eiler et al., 2014) where $\delta'^{33}S=0.515\times\delta'^{34}S$ (with $\delta'^{x}S=\ln[(^{x}S/^{32}S)_{sample}/(^{x}S/^{32}S)_{reference}]$; x=34 or x=33). The $\delta^{x}S$ value is almost identical to $\delta'^{x}S$ ($\delta^{x}S=[(^{x}S/^{32}S)_{sample}/(^{x}S/^{32}S)_{reference}-1]$). However, in the absence of molecular oxygen and ozone (Farquhar et al., 2001), UV-light interaction with SO_2 molecules generates anomalous sulfur isotopic compositions, ($\delta'^{33}S\neq0.515\times\delta'^{34}S$) usually described as "mass-independent fractionations" (MIF) or "mass-anomalous fractionation" (MAF), reported as $\Delta^{33}S$ ($\Delta^{33}S=\delta'^{33}S-0.515\times\delta'^{34}S$). We use here the broader expression "MAF" as such signatures could arise from a mass fractionation law different from the reference law rather than from truly mass-independent processes.

The unusual sulfur isotope abundances, or MAF, provide a strong line of evidence for an Archean atmosphere free of O_2 (Pavlov and Kasting, 2002). Beyond recognizing that $\Delta^{33}S \neq 0$, knowing which species carry the positive and negative $\Delta^{33}S$ anomalies can help determine which process (or processes) and UV wavelengths generated MAF in the distant past. In order to explain the exact structure of MAF data, gases other than SO_2 must be present in the Archean atmosphere. As a result, these data can help us to understand which gases contributed to sustain a sufficient greenhouse effect on the early Earth, such as CH_4 or NH_3 (Zahnle et al., 2006; Domagal-Goldman et al., 2008; Zerkle et al., 2012; Izon et al., 2017). Understanding the exact processes that produced the Archean MAF and describing the underlying mass fractionation law(s) are therefore of significant value.

As soon as the MAF signatures were discovered (Farquhar et al., 2000), SO_2 photolysis lab experiments attempted to undercover the mechanisms that generated them (Farquhar et al., 2001). Many mass fractionation mechanisms have been explored through photochemistry experiments under different UV wavelengths and atmospheric compositions (Masterson et al., 2011; Whitehill and Ono, 2012; Ono et al., 2013; Whitehill et al., 2013; Whitehill et al., 2015; Endo et al., 2016). These experimental approaches have been supplemented with 1-D column atmosphere models and isotopologue cross-section adsorption calculations (Lyons, 2007; Danielache et al., 2008; Lyons, 2009; Ueno et al., 2009; Claire et al., 2014; Endo et al., 2015; Izon et al., 2017; Endo et al., 2019). Overall, the photochemical processes generating S-MAF can in principle be differentiated based on the wavelengths reacting with SO_2.

(1) At wavelengths between 190 and 220 nm, photolytic processes ($SO_2 \rightarrow SO+O$), self-shielding of SO_2 (SO_2 absorbs the wavelengths with which it interacts) and/or pressure-broadening all occur (Lyons, 2009; Ono et al., 2013; Lyons et al., 2018; Endo et al., 2019). Early SO_2 photolysis experiments at 193 nm generated negative-MAF sulfate (ArF excimer laser; Farquhar et al., 2001), focusing attention to this range of wavelengths. MAF-bearing sulfur species are produced because the photodissociation rates are a function of absorption cross-sections, slightly different for each SO_2 isotopologue. In addition, $^{32}SO_2$, the most abundant isotopologue, has a lower self-shielding reaction rate, with a dependence on SO_2 concentrations: the more SO_2 there is, the faster $^{32}SO_2$ shields itself (Lyons, 2009; Ueno et al., 2009; Ono et al., 2013; Endo et al., 2019). SO_2 is photolyzed to SO, which then carries a positive $\Delta^{33}S$ isotopic anomaly and this signal is transferred

to S^0 or possibly COS in the presence of CO. By mass-balance, the exiting SO_3 molecules should carry a negative anomaly. Subsequent oxidation of SO_3 generates sulfuric acid (H_2SO_4) aerosols carrying the negative $\Delta^{33}S$ anomaly that can then be transferred to the oceans. Paired with negative $\Delta^{33}S$ Archean barite and positive $\Delta^{33}S$ Archean pyrite, these experiments formed the basis for the original sulfur photochemical model on early Earth.

(2) At wavelengths between 250 and 350 nm, photoexcitation ($SO_2 \rightarrow {}^*SO_2$) occurs (Ueno et al., 2009; Halevy, 2013; Whitehill et al., 2013; Endo et al., 2019). MAF is produced during the transition of SO_2 from an excited singlet state $^1SO_2$ (the spin of the excited electron is paired with that of the lowest, or ground, energy state) to an excited triplet state $^3SO_2$ (where the excited electron spin is no longer paired with the ground state electron) and the anomaly can then be transferred to either the reduced or oxidized species after reaction with ground SO_2 (Whitehill and Ono, 2012). Initial experiments with continuous wavelengths above 220 nm (Xe lamp) and KrF excimer laser generated positive-MAF sulfate (Farquhar et al., 2001). In the context of Archean barite with negative-MAF sulfate, these longer wavelengths experiments seemed less relevant to Archean atmospheric chemistry. Furthermore, photoexcitation is considered a very minor pathway (Endo et al., 2016).

(3) Across both ranges of wavelengths, recent lab experiments and numerical models have demonstrated the important role played by the absolute SO_2 concentration and the presence of other trace (COS, CO, etc.) and minor (CO_2, CH_4) gases in setting the sign (+/-) of the MAF anomaly in pyrites (Ueno et al., 2009; Claire et al., 2014; Izon et al., 2017; Endo et al., 2019). In a CO-containing atmosphere, MAF processes could occur from a combination of collision-induced system crossing and self-shielding and therefore a combination of photoexcitation and photooxidation (Whitehill et al., 2013; Endo et al., 2016), which is hypothesized to match the measured $\Delta^{36}S/\Delta^{33}S$ ratio. During photoexcitation in the 250-350 nm region, the intersystem crossing from an excited singlet state $^1SO_2$ to an excited triplet state SO_2 ($^*SO_2$) generates $^*SO_2$ with a positive $\Delta^{33}S$ through near-resonant spin coupling between both excited states (Whitehill et al., 2013). This anomaly is expected to be transferred to SO, and not to SO_3, through the reaction ${}^*SO_2+SO_2 \rightarrow {}^*SO+SO_3$, therefore delivering it ultimately to the reduced sulfur pool. But if the anomaly is captured as COS, it could be transferred to sulfate instead (Savarino et al., 2003; Whitehill and Ono, 2012). Experimental results are very sensitive to the initial conditions and to

the overall composition of the artificial atmosphere. This is true in both older and more recent experiments. For example, CO is required to transfer the positive anomaly to COS (Endo et al., 2019) and therefore the final result depends on the initial CO concentration in the reaction volume.

Based on the initial laboratory experiments of SO_2 irradiated by UV light, it was hypothesized that reduced sulfur species carried a positive $\Delta^{33}S$ value and that higher-valent sulfur species (SO_3, SO_4^{2-}) carried a commensurate negative counterpart (e.g. Farquhar et al., 2001). The cascade of reactions that subsequently occurred in the atmosphere would have transferred the positive $\Delta^{33}S$ of reduced sulfur ultimately to pyrite, explaining the generally positive values measured in sedimentary pyrites (Farquhar et al., 2013; Halevy, 2013). Pyrite is proposed to be formed through two different pathways. The first one is direct deposition of elemental sulfur chains S_8 (e.g. Ono et al., 2009a). Elemental sulfur can either produce pyrite following chemical reaction with ferrous sulfide (Rickard, 1975), or following further reduction through microbial disproportionation (e.g. Philippot et al., 2007; Farquhar et al., 2013). In both cases, pyrites would carry the atmospheric reduced sulfur MAF (usually assumed to be positive). The second pathway is through microbial sulfate reduction (MSR) that reduces sulfate to sulfide, which would produce pyrite that carries the atmospheric oxidized sulfur MAF (usually assumed to be negative). MSR is assumed to have started possibly 3.5 Ga ago (e.g; Shen et al., 2001; Ueno et al., 2008; Shen et al., 2009). However, it has been recently suggested that MSR would have evolved only 2.7 Ga ago and that organic sulfur played a major role in the pre-2.7 Ga sulfur cycle (Fakhraee and Katsev, 2019). Even if it was relatively recently-evolved, MSR would have been active during the deposition of the Campbellrand-Malmani platform. In the end, such a model would result in sulfate carrying a negative $\Delta^{33}S$ value and pyrites carrying either positive or negative $\Delta^{33}S$ values.

Finally, geological support for a model where reduced sulfur carries the positive atmospheric MAF signature came from negative $\Delta^{33}S$ values measured in Paleoarchean barites from South Africa, India and Australia (Bao et al., 2007; Philippot et al., 2007; Ueno et al., 2008; Shen et al., 2009; Philippot et al., 2012; Roerdink et al., 2012; Muller et al., 2016) and slightly negative MAF measured in Archean volcanic massive sulfide deposits (Jamieson et al., 2013). Additional evidence interpreted within the frame of the canonical model came from the observation of diamond-hosted sulfides carrying a negative $\Delta^{33}S$ and interpreted as the evidence of Archean biogenic pyrite recycled through the mantle (Cabral et al., 2013). Measurements within single

grains of Archean pyrites revealed a roughly constant and negative $\Delta^{33}S$ in pyrites with a broad range of $\delta^{34}S$ values (Farquhar et al., 2013; Fischer et al., 2014; Zhelezinskaia et al., 2014). To be consistent with the view that oxidized sulfur species carried a negative $\Delta^{33}S$ value, the previous studies suggested that there was mass-dependent microbial reduction of negative $\Delta^{33}S$ sulfate. However, scatter in $\delta^{34}S$ values is also observed in pyrite grains with a positive $\Delta^{33}S$ value (Fischer et al., 2014). Questions remain about Archean MAF processes. Experiments highlight the many possible pathways involved in forming Archean-like MAF signals (e.g. Savarino et al., 2003; Whitehill et al., 2013; Endo et al., 2016). Recently, new theoretical considerations of atmospheric chemistry underlined that the role given to COS as a potential exit channel may have been excessive (Babikov, 2017; Babikov et al., 2017; Harman et al., 2018). They support instead that sulfur was exiting the atmosphere as elemental sulfur chains (S_x) of different sizes and not S_8 exclusively. This theory predicts an exit channel with elemental sulfur carrying *negative* $\Delta^{33}S$ value and sulfate characterized by *positive* $\Delta^{33}S$ values. Obtaining adequate oxidized sulfur from the rock record to measure its MAF value has proven to be challenging.

There is a significantly larger amount of MAF data from Archean pyrites compared to Archean sulfate minerals. Sulfate concentrations in Archean oceans were much lower than today (Grotzinger and Kasting, 1993; Crowe et al., 2014; Fakhraee et al., 2018), leaving only specialized deposits of sulfate minerals (e.g. Bao et al., 2007; Philippot et al., 2012; Roerdink et al., 2012; Ueno et al., 2008). The Paleoarchean barites used to constrain the negative MAF signal derive from volcanoclastic deposits with a petrogenesis that might not lead them to preserve marine sulfate isotopic compositions (Roerdink et al., 2013; Muller et al., 2016; Lowe et al., 2019). In contrast to these older barites, we have observed positive $\Delta^{33}S$ values in younger Neorchean carbonate-associated sulfate (CAS; Paris et al., 2014). CAS is known to derive initially from seawater sulfate in younger successions (e.g. Rennie et al., 2018; Toyama et al., 2020). These observations and models contradict the established paradigm that sulfate carried MAF negative signatures throughout Archean time. Similar observations of positive $\Delta^{33}S$ in CAS had been previously made, but considered as deriving from secondary processes (Domagal-Goldman et al., 2008). There could be a possibility that the Neoarchean CAS that we previously measured is affected by post-depositional processes, as CAS can be potentially altered during diagenesis, metasomatism or sulfate extraction (Gill et al., 2008; Wotte et al., 2012; Rennie et al., 2014; Present et al., 2015; Fichtner et al., 2017; Present et al., 2019).

In this study, we examined the composition and preservation of multiple sulfur isotopes within the sedimentary succession of the Campbellrand-Malmani platform to pinpoint depositional compositions and assess if post-depositional processes have impacted the isotopic composition measured on CAS from samples collected across the platform (Paris et al., 2014). To this end, we sampled different formations that capture different ages, depositional environments, and metamorphic histories across the platform. We utilized the preservation contrast between the better-preserved western part of the craton (Griqualand West structural sub-basin) and the eastern part of the craton (Transvaal basin), where tectonics and the massive plutonic Bushveld Intrusive Complex may have altered the sulfur isotope signals contained in carbonate rocks more strongly than what is observed in Griqualand West (Gleason et al., 2011; Fischer et al., 2014; Johnson et al., 2019). To assess how exhumation and weathering could also have played a role, we compare the signal measured in rocks coming from outcrops to rocks derived from deep diamond drill cores. Finally, to augment our previous study in which only pure carbonates were analyzed, we purposely measured sulfate from various recrystallized and metasomatized samples, including partially silicified samples as well as samples rich in pyrite, to compare how clear post-depositional alteration processes and potential contaminants impacted the CAS sulfur isotopic compositions.

2. Geological context

The Transvaal Supergroup in South Africa is preserved in two distinct structural basins (Griqualand West and Transvaal) and covers over 0.2×10^6 km^2 (Beukes, 1987). Within the Transvaal Supergroup, the Neoarchean Campbellrand-Malmani platform contains attractive targets for micro-CAS analyses with a unique abundance of *in-situ*, benthic carbonate precipitation and the occurrence of extremely diverse stromatolitic and microbialite fabrics (Beukes, 1987; Sumner and Bowring, 1996; Sumner, 1997b; Sumner and Grotzinger, 2004; Knoll and Beukes, 2009). The platform initiated as a carbonate ramp, now preserved as the Schmidtsdrif Subgroup, and developed into a mature rimmed carbonate shelf that spread across the entire Kaapvaal Craton (Sumner and Beukes, 2006) accumulating over 1 km in thickness of marine carbonate. In the Prieska area, deeper basin sediments are preserved and the thickness is ~500 m (Beukes, 1987; Sumner, 1997b). Eventually the carbonate platform drowned during a major transgression that translated into the deposition of iron formations of the Asbestos Hills Subgroup (Kuruman Iron Formation in Griqualand West and the Penge Iron Formation in the Transvaal).

Compared to other Neoarchean strata, the Campbellrand platform is markedly well preserved, particularly in Griqualand West where the strata are flat-lying, and the regional metamorphism is generally low-grade, not exceeding the greenschist facies (200-400°C Miyano and Beukes, 1984; Miyano and Beukes, 1997). The western edge of the craton is marked by thin-skinned folding and faulting, resulting in Campbellrand rocks overthrusting the Proterozoic red beds of the Olifantshoek Group (Beukes, 1987). Petrographic textures in carbonate lithologies from the west reflect this excellent preservation potential as they commonly contain fabric-retentive, early diagenetic dolomite, as well as primary calcite in many areas (Sumner and Grotzinger, 2004; Fischer et al., 2009). To the east, the Transvaal area is marked by steep structural dips, and he Bushveld Igneous Complex intruded the Neoarchean strata *ca.* 2.05 Ga ago (Walraven et al., 1990; Buick et al., 2001), resulting in steeper structure dips, higher metamorphic temperatures, and greater metasomatism than the Griqualand West region (Kaneko and Miyano, 1990; Miyano and Beukes, 1997).

The platform is broadly divided into two large sequences that can be correlated from Griqualand West to the Transvaal (Fig. 1). The first sequence is the Lower Nauga/Reivilo formation while the second one is the Upper Nauga Formation, which is overlain by the Naute/Gamohaan/Frisco formation (Sumner, 1997a; Sumner and Beukes, 2006). Each of them represent aggradational packages separated by a thin transgressive unit at the top of the Lower Nauga/Reivilo formation in the Griqualand West area, the Kamden Iron Formation. Carbonate deposition was reestablished by the time of deposition of the Upper Nauga Formation. The Campbellrand-Malmani platform slope was then at its steepest, with a lagoon that developed episodically behind the reef margin. Immediately after deposition of these facies, a major transgression led to the final demise of the platform, recorded within the Naute/Gamohaan/Frisco formation. In Griqualand West, this flooding is recorded in a sequence characterized by deep subtidal fenestral microbialites with increasing chert content, ultimately grading into the Kuruman Iron Formation. In the Transvaal, the Frisco Formation evolves from ripple marks, cross laminations, and ooids to sequential carbonate/chert layers and finally into the Penge Iron Formation. The Penge and Kuruman Iron formations cap the platform across the entire Kaapvaal Craton.

Sampling was targeted to investigate the sulfur isotope differences between the Griqualand West and Transvaal areas and between formations in the same area of the platform, as well as comparing

the CAS preservation in core versus outcrop samples. As a result, our sulfur isotope data come from samples collected from five different stratigraphic sections through the platform, mostly from cores and outcrops from the Lower Nauga/Reivilo formation and the Naute/Gamohaan/Frisco formation. A few additional samples come from a core through the Monteville Formation. In Griqualand West, the Boetsap section (27° 57.88' S 024° 27.24' E; Truswell and Eriksson, 1973; Sumner, 2002; Sumner and Grotzinger, 2004) captures shallow subtidal paleoenvironments of the Reivilo Formation deposited during the early development of the Campbellrand platform and consists of two parts, Lower (samples WJG1) and Upper Falls (samples W1; Paris et al., 2014). Textures consist of minor grainstones and abundant precipitated stromatolites including seafloor aragonite fans (Sumner and Grotzinger, 2004). Most of the carbonates in this part of the platform have been altered with a fabric-retentive dolomitization, though in this section some horizons are still present as limestone (e.g. Paris et al., 2014). GKP 01 (samples GKP) is a drill core collected with the Agouron Institute South African Drilling Project that penetrates through the proximal slope facies of the Campbellrand platform (Knoll and Beukes, 2009). We targeted cements associated with deep subtidal fenestral microbialites deposited deeper in the basin in the Lower Nauga Formation. SAC samples were collected from the BH1-Sacha core (Altermann and Siegfried, 1997) that captures shallow parts of the platform paleoenvironments. Samples WJG3 and W2 come from the Kuruman Kop section (Sumner, 2002; Sumner and Grotzinger, 2004; 27° 22.82' S 024° 20.82' E) and capture the terminal drowning of the carbonate platform from a shallow lagoonal evaporitic environment (WJG3) to a subtidal microbialite facies that includes abundant early marine cements (W2). The lagoonal facies sediments comprise interbedded fenestrate microbial laminations and isopachously domed limestone (Sumner and Beukes, 2006). The deep subtidal, fenestral microbialite facies of the 2.521 Ga Gamohaan Formation contains abundant herringbone calcite, interpreted as an early seafloor precipitating cement (Sumner and Beukes, 2006; Sumner and Bowring, 1996; Sumner and Grotzinger, 1996). In the Campbellrand platform, herringbone calcite occurs as encrusting beds and is an important phase of void-filling cementation associated with the deep subtidal fenestral microbialites (Sumner and Grotzinger, 1996). Core WB-98 captures the same transition as WJG3 and W2 samples from Kuruman Kop. However, while the facies are similar between WB-98, WJG3 and W2, and all represent the Lower Nauga Formation, most samples in WB-98 contained mm to cm pyrite nodules. We note that such nodules are similar to those investigated in a similar core (Kamber and Whitehouse, 2007). Their presence

makes core WB-98 a poor prospect for accurate CAS measurements due to the enhanced possibility of for oxidized pyrite contamination, but an interesting target for the current investigation. Some samples from this core appeared surficially oxidized at the time of collection, possibly due to the storage conditions (Fig. S4). Thus, WB-98 provides us with an opportunity to test how poor preservation and secondary oxidation of abundant pyrite affects the CAS sulfur isotope signal.

In the Transvaal area, we sampled the Rotterdam Farm section (samples WJG9; 24° 33.643' S ; 027°21.251' E). The Rotterdam Farm section captures the Frisco Formation, a package laterally equivalent to and comprised of similar facies to the Gamohaan Formation. This formation was deposited in a more updip, proximal setting, and like the Gamohaan and Naute formations, the strata record the drowning of the platform, though the Frisco Formation contains more siliciclastic-rich beds than the Gamohaan/Naute formation. The Rotterdam Farm outcrop evolved from a shallow sedimentation environment, as indicated by cross-stratified ooid grainstones, now silicified, to a deeper more quiescent environment and eventually the deposition of the Penge Iron Formation. Rocks in this part of the platform witnessed more deformation and higher temperatures, and the samples we selected contained evidence of both early and late silicification that may have occurred during *ca.* 2.05 Ga Bushveld-related metamorphism and associated hydrothermal fluids circulation (Schiffries and Skinner, 1987). Through these Transvaal area rocks, we were able to explore the effects of metasomatism and metamorphism on the CAS record.

3. Methods

3.1 Sample preparation and petrographic observations

We selected a subset of samples across the various environments and lithologies encountered in the platform. Samples were sectioned using a rock saw, orthogonal to bedding, and polished for petrographic inspection. The slabs were cleaned with MilliQ water, then micromilled using a Sherline 5410 mill equipped with a RoundTool diamond-coated carbide end mill (GR4SI 1/16 D1; 1.5mm diameter) to collect 40 to 150 mg of powders from different petrographic textures. Representative thin sections were made and observed microscopically using polarized and transmitted light (Fig. S1-S3).

3.2 CAS isolation

All plastics (centrifuge tubes, autosampler vials and Biorad columns) were leached in 10% reagent grade HCl and rinsed 5 times in MilliQ water. Teflon vials were cleaned in 5% Seastar HNO_3, rinsed 5 times in MilliQ water, refluxed overnight with concentrated Seastar HNO_3 at 160°C and rinsed 3 times in MilliQ water. For each sample, up to 40 mg of powder were weighed and sonicated for 60 min in 1 M NaCl. All samples were then centrifuged and rinsed 4 times in MilliQ water. After drying, the samples were weighed again, dissolved in 10% HCl, centrifuged, and the supernatant was collected in a Savillex Teflon vial. The supernatant was dried at 120°C on a hot plate under HEPA filtered laminar flow air and the insoluble residue was dried in an oven at 90°C. The residues were weighed, and the dried supernatant was dissolved in HCl. Biorad disposable columns were loaded with 2 ml of clean AG1X8 anion-exchange resin 100-200 mesh (Das et al., 2012; Paris et al., 2014). The resin was then cleaned with 20 ml of 10% HNO_3, 20 ml of 10% HCl and 10 ml of 0.5% HCl. Samples were loaded onto the resin, cations were removed by rinsing the column with 5 times 5 ml of MilliQ water, and sulfate was eluted with 3×4 ml of 0.5 M HNO_3 (Paris et al., 2014). Seawater and corals internal standards were processed through the columns following the same procedures as checks on the consistency of our procedure over time.

3.3 Sulfur isotopes, sulfate concentration, and stable isotope measurements

Sulfur isotopes were measured as $^{32}S^+$, $^{33}S^+$ and $^{34}S^+$ ions at Caltech on a Neptune Plus multi-collector inductively-coupled plasma mass spectrometer (MC-ICPMS, Thermo Fisher Scientific) in high resolution mode. We used a desolvating membrane (Aridus, Cetac) as an introduction system to decrease interferences and make measurements of sulfur possible, following a method described previously (Paris et al., 2013; Paris et al., 2014). Samples were measured by sample-standard bracketing to correct instrumental fractionation. The bracketing standard was a Na_2SO_4 solution concentrated at 20 µmol/l. Na^+ was added to the samples after purification as NaOH to match the sodium concentration of the bracketing standard (Paris et al., 2013). Sulfur isotope ratios of the Na_2SO_4 bracketing solution were determined by comparing it directly to a solution of international standard IAEA-S1 ($\delta^{34}S_{VCDT}$ = -0.3‰, $\delta^{33}S_{VCDT}$ = -0.055‰, (Ding et al., 2001; Ono et al., 2006). The $\delta^{34}S_{VCDT}$ value of our bracketing Na_2SO_4 solution is -1.55‰±0.16 (2sd) and the $\delta^{33}S_{VCDT}$ value is -0.77±0.17‰ ($\Delta^{33}S$ = 0.02±0.17‰) and was determined previously (Paris et al., 2013). All values were corrected assuming linear drift and corrected for instrumental background. $^{33}S/^{32}S$ and $^{34}S/^{32}S$ ratios were corrected independently. We ensure accurate measurement of both

ratios through the consistency or our standards that cover most of the range of $\delta^{33}S$ and $\delta^{34}S$ values measured in our CAS. Consistency standards (seawater and a deep-sea coral aragonite) were purified and measured alongside the Archean carbonates. We measured average $\delta^{34}S$ and $\Delta^{33}S$ values of 20.95 ± 0.19 ‰ and 0.10 ± 0.24‰ for seawater (2sd, n=4) and 22.35± 0.22 ‰ and 0.02 ± 0.22‰ (2sd, n=4) for our coral consistency standards, in agreement with our previous investigations. Individual TPB were measured in each batch of column. We performed the blank corrections using the average of all measured ratios to improve accuracy but using the average concentrations of each batch. In addition to our consistency standards, we added two Paleoproterozoic samples from an economic drill-core (T92/7 and T92/22, Mooidraai Formation, provided by Prof. Beukes, see Fig. 1). Despite their low sulfur content (20 to 180 ppm) similar to the other samples analyzed in this article, they display no MAF values (average $\Delta^{33}S$=0.21±0.30‰, n=3), in agreement with the timing of MAF disappearance evaluated in South Africa (Guo et al., 2009; Luo et al., 2016). Values are presented in the appendix.

In parallel, an aliquot of the purified sample is used to measure sulfate content by ion chromatography at the ESE (Caltech) using a Dionex ICS-3000 system (Thermo Fisher Scientific) using in-house concentration standards to assess accuracy and precision. The CAS concentrations were calculated from the measured sulfate amount, and from the dry weights of the cleaned powder and the insoluble residue. The insoluble residue was evaluated by weighing the centrifuge tube before and after dissolution of the carbonate. The soluble fraction was calculated by difference and evaluated between 22% and 107 % of the initial weight, possibly due to difference of statics from one weighing session to the next. In the absence of a clear way to evaluate uncertainty in these calculations, it was therefore assumed to be 10 % RSD. In a few cases, the soluble fraction could not be evaluated and was assumed to be 95% in order to calculate the CAS concentration of the sample. Because the concentrations were measured after purification, we also applied a blank correction. Total procedural blanks (TPB) were measured as they were run on the Neptune for isotopic ratios. The signal was compared to the bracketing standard to calculate the amount of sulfur. In some cases, more powder than necessary was drilled and duplicates were run from the same dissolved powders.

Uncertainties for sulfur isotopic compositions are given as blank-corrected 2 standard deviations. There are two steps in the blank correction. First, the machine blank from the MC-ICPMS is

subtracted using the signal measured in the blank solution (5% HNO_3+40 µmol/L NaOH to match the Na-addition to the samples). Second, we correct for the total procedural blank (TPB) that includes reagents and sample handling. To measure the TPB we processed empty vials through the whole procedure. Typically there is not enough sulfur to run both the IC and the ICPMS for TPB samples. We evaluated the amount of TPB sulfur on the MC-ICPMS instead. To do so, we diluted the TPB in a known volume of HNO_3+NaOH solution and assumed a linear response of intensity to sulfur concentration, and report the results in the appendix. We used these numbers in the following TBP correction equations as ratios ($^{34}R_{blk}$) and not delta values to correct the isotopic ratio ($^{34}R_{meas)}$ to the true CAS isotopic ratio ($^{34}R_{carb}$:

$$^{34}R_{meas} \times n_{meas} = {}^{34}R_{blk} \times n_{blk} + {}^{34}R_{carb} \times n_{carb} \quad (1),$$

where n_{meas} is the total mass of sulfur from a single sample and

$$n_{carb} = n_{meas} - n_{blk} \quad (2).$$

The true isotopic composition of our sample, $^{34}R^{i}_{carb}$, and concentration of our sample, ppm^{i}_{carb}, were calculated as:

$$^{34}R_{carb} = ({}^{34}R_{meas} \times n_{meas} - {}^{34}R_{blk} \times n_{blk}) / n_{carb} \quad (3)$$

and

$$[SO_4^{2-}]_{carb} = (n_{carb} \times 96.04) / m_{carb} \quad (4),$$

with m_{carb} the carbonate weight of the sample.

An analogous set of equations can be written for evaluating $^{33}R_{carb}$. Uncertainty in the TPB corrected ratio was calculated by propagating the standard deviation obtained for random populations of 1000 values with a normal distribution that has the same evaluated standard deviation as each member of equation (3) and (4). The blank correction increases the typical $\delta^{34}S$ reproducibility from 0.2 to 0.35‰ and the $\Delta^{33}S$ one from 0.40 to 0.70‰ (2sd). Carbon and oxygen isotopes were measured at Caltech using a Delta V Plus isotope ratio mass spectrometer (Thermo Fisher Scientific) equipped with the GasBench II. About 100 µg of powder was weighed and then

digested for at least 2 h at 72°C with 85% phosphoric acid in 12 mL vials pre-flushed with helium. Accuracy was assessed by running two in-house calcite standards at the beginning and end of each analytical session. Reproducibility was monitored by running a Carrera marble standard between every five samples and 0.22‰ for $\delta^{13}C$ and 0.85‰ for $\delta^{18}O$ as 2SD.

3.4 Synchrotron data

We used sulfur K-edge X-ray absorption spectroscopy (XAS) to study the electronic structure and the redox state of the sulfur present in some of the carbonate samples that we analyzed in this study. A few mg of powder were placed onto sulfur-free (< 1 ppm) mylar tape (St. Gobain) in a milled aluminum sample holder. X-ray absorption near edge structure (XANES) spectra for bulk S valence state were collected at beamline 14-3 at Stanford Synchrotron Radiation Lightsource (SSRL) in Menlo Park, California. Samples were measured in fluorescence mode, using a 4-element Vortex detector (Hitachi) equipped with Xspress3 pulse processing electronics (Quantum Detectors). A sodium thiosulfate (NaS_2O_3) standard was used for energy calibration, with the first pre-edge peak (fluorescence maxima) set at 2472.02 eV. Duplicate to quadruplate spectra through the sulfur K-edge were collected for all samples by measuring fluorescence while scanning from 2460 to 2540 eV, and averaged to obtain better spectral resolution and help reduce noise. Repeat analyses of identical spots showed no evidence of redox changes during analysis (e.g. photooxidation by the X-ray beam). We fit the data using the SIXPACK software (Webb, 2005) and the following standards: CAS-sulfate, pyrite, S_8, sulfoxide, sulfonate, methionine, sulfate ester and kerogen type 1 and 2 (Table 1). S_8 was measured from a Sigma-Aldrich alpha-S_8 powder. Pnon yrite, kerogen type 1 and 2, CAS, gypsum and barite were measured from geological samples at SLAC. SO4-ester (dextran sulfate), sulfoxides (methionine sulfoxide), thioether (methionine), sulfonic acids/sulfonate (taurine) were measured as solutions (to minimize the self-absorption artifacts and spectral differences due to crystal packing made up to 30–100 mM in PBS at pH 7.4 (except for dextran sulfate which was analyzed at pH 8.2). Standards are shown in Fig. S5. The relative proportions of each sulfur species are given in Table 1.

4. Results

4.1 Petrographic observations

Samples with a lower degree of post-depositional alteration hail from outcrops and cores located in the better-preserved Griqualand West region (Fig. S1). As previously described (Paris et al 2014), samples from the Boetsap outcrop of the Reivilo Formation (W1, Paris et al., 2014; WJG1, this study) are relatively well-preserved precipitated stromatolites, including aragonite fans, and minor grainstones (Fig. S1a). These rocks have largely been dolomitized but some horizons are still limestone, and they mark the base of the Campbellrand-Malmani platform capturing shallow subtidal paleoenvironments. A new pisolite sample from the Monteville Formation (sample GKP 1175, Fig. S1c-d) supplements our previous data (Paris et al. 2014) from core GKP 01. We note that those samples consist of a very different lithology, dominated by micritized ooids, pisoids, and 'giant' ooids packstone/rudstone. The Kuruman Kop outcrop, with deep subtidal, fenestral microbialite facies, records the terminal carbonate deposition of the drowning platform in the Gamohaan Formation. Samples from this outcrop show micritized oncoids interspersed between drusy to blocky cement, including the early herringbone calcite cement, with rare μm-scale pyrite crystals (Fig. S1b, S2, S3).

The WB-98 drill core also provides a record of the Gamohaan Formation but these strata contain abundant mm to cm pyrite nodules. This sample showed signs of external oxidation that most likely occurred after core extraction and are removed by polishing (Fig. S4), but we cannot exclude that the pyrite minerals were partially oxidized before we handled them. Thus, we characterize the WB-98 samples as less pristine reservoirs for CAS as they contain potentially contaminating sulfides and sulfide-derived sulfate produced during oxidative weathering.

Unlike the Griqualand West area, the Campbellrand-Malmani strata in the Transvaal region were subject to metamorphism and metasomatic fluids introduced by the Bushveld intrusion (Kaneko and Miyano, 1990; Walraven et al., 1990; Buick et al., 2001). Samples collected from outcrops at Rotterdam Farm from the Frisco Formation, equivalent to the Naute/Gamohaan formations, show extensive silicification, including completely quartz-replaced ooids and cherty marble with common euhedral sulfides and silicified veins (Figure S4).

4.2 Geochemical data

The carbonate content of our samples varies from ~10 to ~100 weight percent, reflecting the wide variety of materials analyzed. Carbon and oxygen isotope data are consistent with previous studies

of carbonates from the Campbellrand-Malmani platform (Fischer et al., 2009). The $\delta^{13}C$ values range from -4 to 0.5‰ with most points clustering around -1‰ while $\delta^{18}O$ data range from -18 to -6‰ with most points between -9‰ and -6‰ (Fig. 2).

Our data reveal that almost all CAS samples analyzed are characterized by positive $\Delta^{33}S$ in carbonates with very low sulfate content (Fig. 3, 4, 5). For all samples, the $\Delta^{33}S$ values range from –0.5 ‰ to +8.0 ‰, the $\delta^{34}S$ values range from -7‰ to +25‰ and the sulfate contents range from 1 to >1000 ppm. Almost all the data indicate a CAS content lower than 150 ppm with the exception of two samples from WB-98. A few negative $\Delta^{33}S$ values were encountered but they usually corresponded to the samples with the lowest amount of recovered sulfate (3 nmol or less, for concentrations usually lower than 3 ppm). As a result, the errors make the determined values not significantly different from zero. With the exception of one point from the Boetsap outcrop ($\Delta^{33}S \approx +2$‰, $\delta^{34}S \approx +25$‰), all data follow a positive correlation between the major isotope composition and the ^{33}S anomaly. The $\delta^{34}S$, $\Delta^{33}S$ and CAS measurements agree with our previously published data (Paris et al 2014), but some differences are observed. The highest sulfate contents (>150 ppm) are found in samples from core WB-98, while samples from the Transvaal area display the lowest concentrations (Fig. 4). In addition, the samples from the Boomplaas Formation (core GKP 01) are characterized by less positive $\Delta^{33}S$ values and very negative $\delta^{18}O$. Those samples consist of a very different lithology, dominated by 'giant' ooids.

Overall, our sulfur isotopic data appears to contain three clear endmembers (Fig. 4). Endmember 1 is defined by the most positive $\Delta^{33}S$ values with intermediate CAS content. Endmember 2, on the other hand, reflects samples characterized by $\Delta^{33}S$ values that are either slightly positive or not significantly different from zero and containing low to extremely low CAS content. Finally, Endmember 3 represents samples with the highest sulfate contents and isotopic values with positive to slightly negative $\Delta^{33}S$, but with $\delta^{34}S$ lower values than endmember 1 (as defined by the values from WB-98 samples, purple squares, figs. 3 and 4).

4.3 XANES data

XANES analyses of microdrilled untreated powders reveal sulfur speciation in our samples (Paris et al., 2014). Typical spectral data are shown in Fig. 6 and indicate that sulfur was present in our samples as a mixture between various species of reduced sulfur and sulfate, as expected. For most

of the samples, we obtained a visually satisfactory fit, except for sample WJG3 51. The fit produced a non-existent reduced sulfur peak and failed to fit the shape of the sulfate peak (Fig. S6). The XANES data revealed that most samples contained at least some CAS, in agreement with our previous study (Paris et al., 2014). Most samples also contained sulfate present as SO4-ester, but also traces of gypsum and barite. Kerogen-sulfur was the most abundant reduced sulfur species in our samples and we usually did not detect a lot of pyrite or S_8. In addition, we found presence of sulfonate in two samples and thioether in one sample.

5. Discussion

To understand the sulfur photochemistry and associated sulfur fractionation laws generated by Archean atmospheric processes, most models rely on data from sedimentary pyrites and assume that sulfate exited the atmosphere already carrying a negative $\Delta^{33}S$ value. Existing direct oxidized sulfur data derive primarily from Paleoarchean barites (Bao et al., 2007; Ueno et al., 2008; Shen et al., 2009; Philippot et al., 2012; Roerdink et al., 2012; Muller et al., 2016). These barites were all deposited between 3.5 and 3.1 Ga ago and therefore cover only a small fraction of the Archean Eon. Furthermore, their existence is a something of a paradox for an ocean with low sulfate concentrations where sulfate evaporites are not observed in the rock record (Grotzinger and Kasting, 1993). Thus, the barite may not represent Archean open-ocean sulfate as they are associated with volcaniclastic deposits (Philippot et al., 2012) or reflect hydrothermal systems (Van Kranendonk, 2006). In contrast to the barite record, the data presented here shows an unambiguously positive $\Delta^{33}S$ signal in carbonate-associated sulfate throughout our diverse sample set, consistent with previous results (Paris et al., 2014). Our diverse dataset, ranging from cores to outcrops and from pure carbonate samples to samples with complex mineralogy or preservational history, further reveal seawater sulfate deposition and preservation across the marine carbonate platform captured by the ~2.5 Ga Campbellrand-Malmani sequence. In the following discussion, we first assess if this positive $\Delta^{33}S$ signal is primary or post-depositional. We then compare the CAS data and the pyrite data in the Campbellrand platform and finally discuss the possible atmospheric origin of the positive $\Delta^{33}S$ in CAS.

5.1 Does post-depositional history affect the sulfur isotopic signal?

A positive $\Delta^{33}S$ anomaly in oxidized sulfur species is at odds with most interpretations of the Archean sulfur cycle. We combined the current dataset and our previous data to test whether the omnipresent positive $\Delta^{33}S$ signal that we measured could actually derive from preservational biases or metamorphic history. The data in Fig. 3 indicate that positive $\Delta^{33}S$ values are also correlated with $\delta^{34}S$ values. Fig. 4 shows that, across the entire platform, the sulfate content and $\Delta^{33}S$ values define a domain delimited by three likely endmembers. These are not necessarily mixing relationships, but rather types of samples with characteristic relationships between their sulfur isotope value and sulfate content. The different cores and sections do not appear randomly distributed between these three endmembers and we hypothesize that each of them corresponds to a different phase of the geological history of the platform.

We first ensure that we measured sulfur from CAS. CAS is present in almost all our samples. We also found abundant sulfur both as kerogen and SO_4-ester. We do not expect sulfur from kerogen to contribute to our measured CAS because sulfur extraction from organic matter, especially kerogens, require stronger chemical reagents than those we used for CAS extraction (e.g. Raven et al., 2015). Similarly, pyrite was present only in small amounts in our samples and it is not significantly dissolved in our protocol (Present et al., 2015). S_8 was present in only two of the tested powders. Barite could not have been dissolved during our process, which is also designed to not collect gypsum (Present et al., 2019). However, we cannot exclude that we could have leached sulfate from SO4-ester groups and that our sulfur isotopic composition resulted from a CAS-SO_4 ester mix. Such groups are found for example in brachiopod shell carbonates where they play a role in biomineralization; however, they are not a known diagenetic product (Richardson et al., 2019a; Richardson et al., 2019b). In any case, the sulfate in those groups likely would have initially been derived from seawater sulfate, just like the CAS.

We propose that Endmember 1 (high $\Delta^{33}S$, intermediate [CAS]) records the most pristine original sulfate isotopic composition. This endmember consists primarily of samples from two outcrops located at the base and the top of the platform in the Griqualand West area: Boetsap and Kuruman Kop. Some of the data points were previously published (Paris et al., 2014) and others come from additional sampling from those two locations and new data presented here. Carbonates are preserved as fabric-retentive dolomite or limestone that initially precipitated as seafloor carbonate cements, occasionally associated with microbial mats (Sumner and Beukes, 2006; Sumner and

Bowring, 1996; Sumner and Grotzinger, 1996). Carbon and oxygen isotope data agree with previous investigations (Fischer et al., 2009). We initially chose these samples as the best candidates for retaining Archean CAS because they show no sign of post-exhumation oxidation, they contain only traces of disseminated pyrite, and they display no petrographic evidence of deformation or metamorphic alteration (Paris et al., 2014), only reaching low-grade greenschist facies (Miyano and Beukes, 1984). Overall, the sulfate content of those rocks (roughly 10 to 50 ppm) is consistent with precipitation of inorganic aragonite in seawater with sulfate concentrations around 100 µmol/L or precipitation calcite at concentrations lower than 30 µmol/L (Barkan et al., 2020), a range that agrees with existing seawater sulfate concentration estimates for the Neoarchean (Crowe et al., 2014; Fakhraee et al., 2018). However, no constraints exists on dolomite, or during the aragonite-calcite diagenetic inversion (except during meteoric diagenesis, Gill et al., 2008).

Unlike Endmember 1, we suggest that Endmember 2 (low $\Delta^{33}S$, low [CAS]) documents sulfur isotopes affected by late diagenesis and/or metamorphism and metasomatic fluids. Endmember 2 contains samples from the Rotterdam farm outcrop, both located in the Transvaal area, as well as some samples from the Griqualand West area such as late void-filling spar. The Transvaal area was chosen to assess the influence of post-depositional history as depositional depth and metamorphic history were different between the two parts of the platform, including the Bushveld intrusion *ca.* 2.05 Ga ago (Walraven et al., 1990). Selected locations reached temperatures up to 500°C and contain substantial petrographic evidence of metamorphism (Miyano and Beukes, 1997). Samples from the Rotterdam Farm location were sometimes silicified, preventing us at times from drilling out sample material. Petrographically, they show silicified fractures and extensive replacement of carbonate ooids by chert. Other samples were characterized by low weight percent (<10%) carbonate and CAS content. The samples that were affected by the Bushveld metamorphism have the lowest sulfate content, sometimes close to our total procedural blank. Some of those points can therefore not be represented in Figs 3 and 4 but would likely extend Endmember 2 farther to the right in Fig. 4. We also note that samples WJG9 143 from the Rotterdam farm outcrop is characterized by homogeneous $\delta^{13}C$ values and heterogeneous sulfur isotopic compositions (both $\delta^{34}S$ and $\Delta^{33}S$). Such a pattern is not necessarily surprising if the rocks were initially deposited in a sulfate-poor environment. These results suggest that no massive sulfate overprinting occurred in these rocks. In addition, some samples from Griqualand West

also belong to this endmember. For example, two samples (spar) of GKP 01 from the Lower Nauga/Reivilo Formation are characterized by $\Delta^{33}S$ values close to zero and very low CAS content (less than 5 ppm, Paris et al., 2014). This core did not strongly experience the Bushveld contact metamorphism, however these rocks contain void-filling sparry cements that reflect residual porosity readily accessed by Bushveld hydrothermal fluids (Gleason et al., 2011; Paris et al., 2014). Overall, Endmember 2 shows diagenetic or metamorphic alteration of the rocks that tends to erase the $\Delta^{33}S$-$\delta^{34}S$ trend, not create it. The carbonates might all be secondary and reprecipitated in a fluid that was poor in sulfate. We conclude that these secondary processes do not explain the positive $\Delta^{33}S$ values in Endmember 1.

Endmember 3 (low $\Delta^{33}S$, high [CAS]) is the richest in sulfate and corresponds mainly to samples from the pyrite-rich and secondarily-oxidized core WB-98, and thus we contend that this endmember reflects the effects of incipient oxidative weathering. WB-98 samples have abundant pyrite nodules and showed clear visual signs of surficial oxidation. As a result, they do not represent the ideal target to explore the sulfur isotopic composition of seawater CAS, but could represent a source of sulfate with a positive $\Delta^{33}S$ if we assume that pyrite oxidation is the origin for the CAS measured in our samples. However, WB-98 is characterized by lower $\Delta^{33}S$ and $\delta^{34}S$ values and richer sulfate contents than samples from other locations, likely connected to the presence of (re)oxidized pyrite. We purposefully drilled a pyrite nodule texture as a way to test the influence of the presence of pyrite and to investigate whether the positive $\Delta^{33}S$ could be derived from pyrite oxidation, either in the lab or during the depositional history of the rock. This sample (WB98 998d, Fig. S4, sample marked "Py" in Fig. 3, 4, and 7A) is an outlier. It has by far the highest sulfate content and the most negative $\delta^{34}S$ and $\Delta^{33}S$ values from the entire dataset. The pyrite sample initially contained ~25% of pyrite (10 mg) and we recovered 2.4 µmol SO_4^{2-} (most likely including sulfate from CAS and from oxidized pyrite). If we assume that all the sulfate came from pyrite oxidation, 2.4 µmol SO_4^{2-} would correspond to the oxidation of ~150 µg of pyrite (~1.5% of the pyrite included in our drill sample). We cannot determine however whether such oxidation occurred in the core prior to sampling or in the lab after sampling. The former is likelier than the latter as our protocol is not able to oxidize pyrite to such an extent (Present et al., 2015). Regardless, sulfate from pyrite oxidation clearly overprinted the sulfur signals of WB-98 if it started with a composition near Endmember 1. If correct, pyrite contamination lowers the measured isotopic composition and does *not* generate the positive signal we see in Endmember 1,

especially in this part of the platform where nodular pyrites are documented as having negative $\Delta^{33}S$ (Fischer et al., 2014).

The rest of the samples falls between the three endmembers. This includes part of the samples from Kuruman Kop, Boetasp, core BH1-Sacha, GKP-01. In particular, samples from the Boomplaas Formation (core GKP 01) are characterized by less positive $\Delta^{33}S$ values than endmember 1 and very negative $\delta^{18}O$. Because they are the only samples from this formation, we cannot draw any specific conclusion; however we note that those samples are lithologically unique within our sample set, consisting of coarse sand to gravel-sized ooid, pisoid, and 'giant' ooid packstone (Fig. S1). However, it is difficult to interpret the extent to which samples between the endmembers represent, or not, a combination of the processes mentioned previously.

As an alternative hypothesis to Endmember 1 being a pristine record of marine sulfate, we considered if Endmember 1 could reflect the oxidation of disseminated positive-MAF pyrites in the absence of negative MAF nodules. Most disseminated pyrites exhibit positive MAF values (Ono et al., 2009a; Ono et al., 2009b) and their oxidation would tend to increase $\Delta^{33}S$ values of sulfate. However, XANES results indicate that our Endmember 1 samples do contain CAS (Fig. 6), and only have rare to extremely rare disseminated pyrites, as confirmed by direct observations of the thin sections matching the drilled areas performed for some of the samples (Fig. S1, S2, S3). Therefore, in Endmember 1 samples, the sulfate we measure could either be purely CAS, or a mixture of CAS and oxidized disseminated pyrite. For example, XANES data reveal that sample W1-5 contains ~10% sulfur in sulfate and the rest as pyrite (~75%) or organic (~15 %) sulfur, yielding $\Delta^{33}S$ values as high as +10.4 ‰ (Paris et al. 2014). If we assume that the $\Delta^{33}S$ value of sulfate should be close to Eoarchean barites (i.e. lower than -0.5‰), this means our measured $\Delta^{33}S$ would require the contribution of oxidized pyrites with values of $\Delta^{33}S$ higher than +11.6‰. Such high $\Delta^{33}S$ values have not been documented in contemporaneous pyrites (Fig. 7). The highest published value of disseminated pyrite in the Reivilo Formation is $\Delta^{33}S$ = +10.34‰ (Izon et al., 2015), with the exception of pyrites from the Fig Tree Group ($\Delta^{33}S$ values up to 14‰), but they would be an unlikely candidate as a source of sulfur to the basin because they are characterized by negative $\delta^{34}S$ values, lower than -20‰ (Philippot et al., 2012). Thus the published pyrite data do not support such a mixing, even assuming all pyrite is oxidized during sample preparation. The fact that pyrite and CAS isotopic compositions do not overlap in the Gamohaan formation (from

the better-preserved Kuruman Kop section) further supports that CAS sulfur isotope data from Endmember 1 do not reflect procedural pyrite oxidation, as further discussed in section 5.2. As a result, we feel confident that Endmember 1 likely contains the most pristine CAS in the platform. We therefore assume that this positive $\Delta^{33}S$ signal reflects sulfate incorporated in the rocks during their precipitation from seawater as early cements across the Neoarchean platform, in agreement with our previous interpretation (Paris et al., 2014).

5.2 How could $\Delta^{33}S$-positive sulfate form?

There are at least three potential ways to explain how seawater sulfate in the Campbellrand basin can exhibit positive $\Delta^{33}S$ values. (1) The marine sulfate in the waters overlying the Campbellrand-Malmani platform could be dominated by sulfate coming from oxidative weathering of positive $\Delta^{33}S$ pyrite, (2) microbial metabolisms (sulfur disproportionation or sulfur oxidation) led to forming sulfate with positive $\Delta^{33}S$ values or (3) Neoarchean atmospheric processes could have generated original sulfate with a positive $\Delta^{33}S$.

(1) In order to create sulfate with positive MAF signature, we could consider oxidative weathering of positive $\Delta^{33}S$ pyrites during the Archean. First, this idea is in conflict with the observation of unoxidized detrital pyrites in underlying and overlying strata (Johnson et al., 2014). Even in a fully oxygenated atmosphere, modern weathering of Archean crust with anomalous $\Delta^{33}S$ pyrite produces sulfur with no MAF (Torres et al., 2018). For Archean weathering to generate sulfate with a positive $\Delta^{33}S$ value, oxidation of the S-species carrying only the positive $\Delta^{33}S$ signal is required. In addition, highly positive $\Delta^{33}S$ pyrites such as the values found in our CAS measurements are only found in the latest Neoarchean pyrites, suggesting that this weathering would need to involve contemporaneous pyrites from the Campbellrand platform, which is difficult to envision. It has been suggested that biologically-mediated weathering of sulfur minerals could have started about 2.7 Ga ago (Stüeken et al., 2012), which could possibly be reconciled with detrital pyrite observations assuming differential pyrite weathering using a biological oxidant other than O_2. In sum, we suggest that Archean oxidation of pyrites is inconsistent with both modern and ancient observations of pyrite weathering.

(2) An alternative explanation for the positive $\Delta^{33}S$ values measured in sulfate to be produced as a result of oxidation of more reduced sulfur species would be microbially-mediated sulfide oxidation

to sulfate at the time of rock formation, or sulfur-disproportionation (e.g. Philippot et al., 2007; Shen et al., 2009; Farquhar et al., 2013). Microbial activity is expected in Noeoarchean basins (e.g. Farquhar et al., 2013), especially in the case of samples from cores GKP 01 and WB-98 or from the Kuruman Kop outcrop, where microbial fenestrae and rolled microbial mats are observed (e.g. Fig. S4). If we follow the canonical model and assume that atmospheric sulfate carries a negative $\Delta^{33}S$, the positive $\Delta^{33}S$ isotopic compositions we measure in Neoarchean CAS would imply that sulfate derived from sulfide oxidation or elemental sulfur disproportionation completely erased the isotopic signature of the atmospheric input in the Campbellrand-Malmani basin. We do not ever measure negative CAS $\Delta^{33}S$ in pristine samples. Our observation implies that seawater sulfate in this basin did not carry a negative $\Delta^{33}S$ value, regardless of the atmospheric processes involved.

(3) Instead, we argue that the positive MAF values in CAS result from atmospheric processes that generate an oxidized sulfur species carrying the positive $\Delta^{33}S$ anomaly, with reduced sulfur in early diagenetic disseminated pyrites deriving from microbial reduction of this sulfate. Outcrop samples reveal $\Delta^{33}S$ values that are more positive than those measured from core samples. However, cores and outcrops do not cover the same formations and we cannot interpret this difference in detail. However, because we have the most data for samples from Boetsap and Kuruman Kop, both outcrops from different locations of the Griqualand West part of the platform (bottom and top of the Campbellrand-Malmani platform, respectively), we investigate the relationship between $\delta^{34}S$ and $\Delta^{33}S$ for these two suites of samples, including previous data (Paris et al., 2014). Fig. 7 shows that in a $\delta^{34}S$ vs. $\Delta^{33}S$ crossplot, most of the data from the Gamohaan (top of the platform, Kuruman Kop outcrop, Fig. 7A) and the Reivilo Formation (base of the platform, Boetsap outcrop, Fig. 7B) plot along straight lines. The slope of this line is identical, within error, to the Archean array, initially defined by bulk rock measurements ($\delta^{34}S=0.89\times\Delta^{33}S$; Ono et al., 2009a) and attributed to MAF formation by interaction of UV-light with SO_2 molecules. We also note that the Gamohaan Formation, as recorded by the better-preserved Kuruman Kop, contains CAS and pyrite data that do not overlap with each other, reinforcing our interpretation that we did not simply measure reduced sulfur that would have been reoxidized during rock handling. The isotopic relationships between these two phases may reflect different aspects of environmental processes. In the Reivilo formation, almost all of the CAS data strictly follow the Archean array, outside of one point with a very high $\delta^{34}S$, while pyrite data from previous

publications are more varied (Fig 7B). If the original oxidized sulfur species in seawater had a positive $\Delta^{33}S$, then sulfur dioxide gas emitted from the mantle with $\Delta^{33}S \approx 0‰$ experienced atmospheric photochemical reactions that led to positive $\Delta^{33}S$ sulfate. Presumably the negative $\Delta^{33}S$ would be carried in the resulting reduced sulfur species. Part of the positive $\Delta^{33}S$ sulfate could have then been reduced through a mass-dependent reduction process, such as microbial sulfate reduction (double-headed arrow in Fig. 7), to be preserved as sedimentary pyrites carrying positive $\Delta^{33}S$ values – forming the Archean pyrite array. Disseminated pyrite crystals could also be formed secondarily or altered by later processes, such as disseminated pyrite from shales adjacent to the Campbellrand platform that were characterized magnetically as secondary (Fischer et al., 2014). These MDF processes such as microbial and thermochemical sulfate reduction do not affect the $\Delta^{33}S$ value and could explain why the $\delta^{34}S$ data of reduced sulfur covers a wider range than the CAS data.

Our hypothesis that positive-MAF was carried by oxidized sulfur species and negative MAF was hosted by reduced sulfur species would explain why positive $\Delta^{33}S$ can be found in both disseminated pyrite and CAS, as well as why negative values are found only in pyrites across the Campbellrand platform and not in CAS. Within this framework, we interpret the CAS sulfur isotopes in the Gamohaan Formation as reflecting the non-quantitative formation of pyrite. As a result, sulfate would keep its initial $\Delta^{33}S$ positive trend, but the $\delta^{34}S$ values of the sulfate would be offset from pyrite towards positive values. We indeed observed a positive offset of ~5‰ from sulfate to pyrite in the Gamohaan Formation (Fig. 7A), which is small yet consistent with microbial sulfate reduction (Crowe et al., 2014). The observation of such an offset in the Gamohaan formation rich in microbial mats, unlike its observation in the Reivilo formation where no such mats are observed, would be consistent with microbial processes occurring. The overall relationship between sulfate and pyrite in all measurements of the Campbellrand platform is consistent with the hypothesis that disseminated pyrites formed from sulfate carrying a positive $\Delta^{33}S$ value.

This observed sulfate-sulfide relationship emphasizes the fact that the only samples revealing clearly negative $\Delta^{33}S$ are nodular or layered pyrites while the disseminated pyrites tend to display positive values in existing data for the Campbellrand-Malmani platform (Kamber and Whitehouse, 2007; Farquhar et al., 2013; Fischer et al., 2014). Within the Reivilo formation, pyrites with

negative $\Delta^{33}S$ values and very negative $\delta^{34}S$ values seem to indicate that there was a process with a distinct MAF law (oval, Fig. 7), and not a simple MDF process with initial sulfate containing a negative $\Delta^{33}S$. Therefore, we suggest that these pyrites could derive from atmospherically-derived negative $\Delta^{33}S$ reduced sulfur with positive $\Delta^{33}S$ sulfide derived from sulfate to make pyrite (ferrous sulfide reacting with elemental sulfur to make pyrite, Rickard 1975).

5.3 Can atmospheric processes generate positive sulfate?

This positive $\Delta^{33}S$ atmospheric sulfate hypothesis leaves us with the challenge of explaining the possibility of a ^{33}S-enrichment in sulfate that contradicts the barite record. Laboratory and numerical experiments have produced different fractionations including some showing that oxidized S-phases can carry a positive $\Delta^{33}S$. Overall, no lab experiment seems to directly capture the Archean relationship observed between $\delta^{34}S$, $\Delta^{33}S$ and $\Delta^{36}S$ ($\Delta^{36}S/\Delta^{33}S \sim 1$ in sediments), which demonstrates that open and critical questions remain about the underlying MAF-generating process.

Until recently, in light of only one sulfate archive (barites), previous studies that resulted in modeled or experimental positive $\Delta^{33}S$ sulfate were disregarded. The first models based on cross-section adsorptions yielded positive anomalies in sulfate (Ueno et al., 2009). This result was considered unfit to explain the Archean MAF signature. Ueno et al. (2009) thus developed the idea that the presence of COS in the atmosphere shielded part of the photolysis spectrum in order to generate a negative anomaly, because COS preferentially absorbs wavelengths between 200 and 210 nm. During photooxidation in the 180-220 nm region, the predicted photolytic processes yield $\Delta^{33}S$ values whose sign depends strongly on the cross-section adsorption profiles. The initial sign of the MAF signal in sulfate was calculated as positive (Claire et al., 2014) but then changed to negative using revised spectra (Endo et al., 2015; Izon et al., 2017). By contrast, because the latest cross-sections produce fractionation that appear in agreement with negative sulfate (Endo et al., 2015; Izon et al., 2017), no additional calculations have been produced to understand if the presence of other gases could affect the UV spectrum and lead to positive sulfate formation. However, two other known processes can create a positive $\Delta^{33}S$ in sulfate. Photooxidation without self-shielding can create sulfate with a (small) positive $\Delta^{33}S$ (Endo et al., 2016). Fractionation during S_x sulfur chain formation (Babikov, 2017; Babikov et al., 2017) also creates positive $\Delta^{33}S$

values in sulfate. This result stems from the unlikelihood of combining 2 minor isotopes in one chain and that S_4 and S_8 should therefore carry a negative $\Delta^{33}S$ value (Harman et al., 2018).

If Archean atmospheric processes did produce sulfate with positive $\Delta^{33}S$, then the negative $\Delta^{33}S$ values in rare Paleoarchean barite might be better understood as an exception rather than the norm. These barites might have precipitated following increased sulfate deposition during intensive volcanic events, as suggested by microanalytical Secondary Ion Mass Spectrometry measurements of sulfur isotopes (Philippot et al., 2012; Muller et al., 2016), though the interpretation of a volcanic array remains equivocal (Roerdink et al., 2013). During these events, the SO_2 emitted by volcanoes could be affected by photooxidation processes in the SO_2- and COS-rich plume. As explored rigorously, photooxidation processes at high COS concentration are expected to generate sulfate aerosols carrying a negative $\Delta^{33}S$ (Ueno et al., 2009; Muller et al., 2016), possibly with a contribution of self-shielding, though excessive partial pressure of SO_2 could lead to MAF suppression (Endo et al., 2019). Therefore, there is a likely possibility that sulfate deposited during such intense volcanic events carried an isotopic composition different than the 'normal' background sulfate aerosol deposition. During volcanic events, the presence of potential oxidants may change or there may be self-shielding and/or shielding by OCS as SO_2 concentrations locally increase. In addition, barites are not characterized by homogeneously negative $\Delta^{33}S$ values as some of them carry a less negative to slightly positive MAF (Muller et al., 2016). Observations of such heterogeneities raise the possibility that sulfate deposition is not characterized by a constant negative anomaly, which has also been suggested by other studies (Ueno et al., 2009; Claire et al., 2014; Paris et al., 2014; Harman et al., 2018). If correct, CAS would record the 'normal' MAF law under an optically thin atmosphere in contrast to the barite deposits recording processes such as self-shielding that occurred during volcanic events. Alternatively, different processes could occur during different period of the Archean, similar to previous suggestions of atmospheric composition oscillations or secular changes (e.g. Domagal-Goldman et al., 2008; Izon et al., 2015; Ueno et al., 2009), and sulfate aerosols could be positive at times and negative at others.

6. Conclusion

The Campbellrand-Malmani carbonate platform provides useful constraints on the isotopic compositions of seawater sulfate and offers unique insights into Neoarchean sulfur cycling. The

platform offers contrasting degrees of preservation of both pyrite and sulfate-bearing lithologies. We used this diverse record to explore the quality of the Archean CAS archive, and hone interpretations of the Neoarchean sulfur cycle. The data show that sulfate incorporated into and preserved in carbonates (CAS) records a positive $\Delta^{33}S$ value that cannot be explained through secondary processes or contamination from pyrite. We found no sulfate carrying a negative $\Delta^{33}S$ deposited across this 150-million-year interval of time. This apparent contradiction with negative $\Delta^{33}S$ recorded in Paleoarchean barites and many current assumptions about the Archean sulfur cycle that require negative $\Delta^{33}S$ sulfate could reflect a secular change in the nature of atmospheric composition and/or photochemical processes affecting sulfur isotopes from early to late Archean time, or suggest that the previously-studied barites record a different suite of processes associated with a unique and rare depositional environment, and/or that early diagenetic and metasomatic sulfur cycling commonly controls pyrite MAF signatures. Our recent CAS results further indicate that Neoarchean atmospheric processes could have produced sulfate with a positive $\Delta^{33}S$ value, and therefore the mechanisms that lead to positive-MAF sulfate need to be further explored to better constrain the composition of the Archean atmosphere.

Acknowledgments

We thank Dr. LaFlamme, Dr. Marin-Carbonne and one anonymous reviewer for their helpful reviews and Prof. Ono for handling the editorial process. Altogether, they helped us improve this article. We thank Prof. Beukes for his help in accessing the cores and for feedback on the geological context. Use of the Stanford Synchrotron Radiation Lightsource, SLAC National Accelerator Laboratory, is supported by the U.S. Department of Energy, Office of Science, Office of Basic Energy Sciences under Contract No. DE-AC02-76SF00515. Financial support was received from the NSF (grant EAR-1349858 attributed to WWF and JFA). WWF acknowledges support from the Simons Foundation Collaboration on the Origins of Life.

Altermann W. and Siegfried H. P. (1997) Sedimentology and facies development of an Archaean shelf: carbonate platform transition in the Kaapvaal Craton, as deduced from a deep borehole at Kathu, South Africa. *J. Afr. Earth Sci.* **24**, 391-IN4.

Babikov D. (2017) Recombination reactions as a possible mechanism of mass-independent fractionation of sulfur isotopes in the Archean atmosphere of Earth. *Proc. Natl. Acad. Sci.* **114**, 3062.

Babikov D., Semenov A. and Teplukhin A. (2017) One possible source of mass-independent fractionation of sulfur isotopes in the Archean atmosphere of Earth. *Geochim. Cosmochim. Acta* **204**, 388–406.

Bao H., Rumble III D. and Lowe D. R. (2007) The five stable isotope compositions of Fig Tree barites: Implications on sulfur cycle in ca. 3.2 Ga oceans. *Geochim. Cosmochim. Acta* **71**, 4868–4879.

Barkan Y., Paris G., Webb S. M., Adkins J. F. and Halevy I. (2020) Sulfur isotope fractionation between aqueous and carbonate-associated sulfate in abiotic calcite and aragonite. *Geochim. Cosmochim. Acta*. Available at: http://www.sciencedirect.com/science/article/pii/S0016703720301939.

Beukes N. J. (1987) Facies relations, depositional environments and diagenesis in a major early Proterozoic stromatolitic carbonate platform to basinal sequence, Campbellrand Subgroup, Transvaal Supergroup, Southern Africa. *Sediment. Geol.* **54**, 1–46.

Blättler C. L., Kump L. R., Fischer W. W., Paris G., Kasbohm J. J. and Higgins J. A. (2017) Constraints on ocean carbonate chemistry and pCO2 in the Archaean and Palaeoproterozoic. *Nat. Geosci* **10**, 41–45.

Buick I. S., Maas R. and Gibson R. (2001) Precise U–Pb titanite age constraints on the emplacement of the Bushveld Complex, South Africa. *J. Geol. Soc.* **158**, 3.

Cabral R. A., Jackson M. G., Rose-Koga E. F., Koga K. T., Whitehouse M. J., Antonelli M. A., Farquhar J., Day J. M. D. and Hauri E. H. (2013) Anomalous sulphur isotopes in plume lavas reveal deep mantle storage of Archaean crust. *Nature* **496**, 490–493.

Claire M. W., Kasting J. F., Domagal-Goldman S. D., Stüeken E. E., Buick R. and Meadows V. S. (2014) Modeling the signature of sulfur mass-independent fractionation produced in the Archean atmosphere. *Geochim. Cosmochim. Acta* **141**, 365–380.

Crowe S. A., Paris G., Katsev S., Jones C., Kim S.-T., Zerkle A. L., Nomosatryo S., Fowle D. A., Adkins J. F., Sessions A. L., Farquhar J. and Canfield D. E. (2014) Sulfate was a trace constituent of Archean seawater. *Science* **346**, 735–739.

Danielache S. O., Eskebjerg C., Johnson M. S., Ueno Y. and Yoshida N. (2008) High-precision spectroscopy of 32S, 33S, and 34S sulfur dioxide: Ultraviolet absorption cross sections and isotope effects. *J. Geophys. Res. Atmospheres* **113**, D17314.

Das A., Chung C.-H., You C.-F. and Shen M.-L. (2012) Application of an improved ion exchange technique for the measurement of d34S values from microgram quantities of sulfur by MC-ICPMS. *J. Anal. At. Spectrom.* **27**, 2088–2093.

Ding T., Valkiers S., Kipphardt H., De Bièvre P., Taylor P. D. P., Gonfiantini R. and Krouse R. (2001) Calibrated sulfur isotope abundance ratios of three IAEA sulfur isotope reference materials and V-CDT with a reassessment of the atomic weight of sulfur. *Geochim. Cosmochim. Acta* **65**, 2433–2437.

Domagal-Goldman S. D., Kasting J. F., Johnston D. T. and Farquhar J. (2008) Organic haze, glaciations and multiple sulfur isotopes in the Mid-Archean Era. *Earth Planet. Sci. Lett.* **269**, 29–40.

Eiler J. M., Bergquist B., Bourg I., Cartigny P., Farquhar J., Gagnon A., Guo W., Halevy I., Hofmann A., Larson T. E., Levin N., Schauble E. A. and Stolper D. (2014) Frontiers of stable isotope geoscience. *Chem. Geol.* **372**, 119–143.

Endo Y., Danielache S. O. and Ueno Y. (2019) Total Pressure Dependence of Sulfur Mass-Independent Fractionation by SO2 Photolysis. *Geophys. Res. Lett.* **46**, 483–491.

Endo Y., Danielache S. O., Ueno Y., Hattori S., Johnson M. S., Yoshida N. and Kjaergaard H. G. (2015) Photoabsorption cross-section measurements of 32S, 33S, 34S, and 36S sulfur dioxide from 190 to 220 nm. *J. Geophys. Res. Atmospheres* **120**, 2546–2557.

Endo Y., Ueno Y., Aoyama S. and Danielache S. O. (2016) Sulfur isotope fractionation by broadband {UV} radiation to optically thin {SO2} under reducing atmosphere. *Earth Planet. Sci. Lett.* **453**, 9–22.

Fakhraee M., Crowe S. A. and Katsev S. (2018) Sedimentary sulfur isotopes and Neoarchean ocean oxygenation. *Sci. Adv.* **4**, e1701835.

Fakhraee M. and Katsev S. (2019) Organic sulfur was integral to the Archean sulfur cycle. *Nat. Commun.* **10**, 4556.

Farquhar J., Bao H. and Thiemens M. (2000) Atmospheric Influence of Earth's Earliest Sulfur Cycle. *Science* **289**, 756–758.

Farquhar J., Cliff J., Zerkle A. L., Kamyshny A., Poulton S. W., Claire M., Adams D. and Harms B. (2013) Pathways for Neoarchean pyrite formation constrained by mass-independent sulfur isotopes. *Proc. Natl. Acad. Sci.* Available at: http://www.pnas.org/content/early/2013/02/13/1218851110.abstract.

Farquhar J., Savarino J., Airieau S. and Thiemens M. H. (2001) Observation of wavelength-sensitive mass-independent sulfur isotope effects during SO2 photolysis: Implications for the early atmosphere. *J. Geophys. Res. Planets* **106**, 32829–32839.

Fichtner V., Strauss H., Immenhauser A., Buhl D., Neuser R. D. and Niedermayr A. (2017) Diagenesis of carbonate associated sulfate. *Chem. Geol.* **463**, 61–75.

Fischer W. W., Fike D. A., Johnson J. E., Raub T. D., Guan Y., Kirschvink J. L. and Eiler J. M. (2014) SQUID–SIMS is a useful approach to uncover primary signals in the Archean sulfur cycle. *Proc. Natl. Acad. Sci.* **111**, 5468–5473.

Fischer W. W., Hemp J. and Johnson J. E. (2016) Evolution of Oxygenic Photosynthesis. *Annu. Rev. Earth Planet. Sci.* **44**, 647–683.

Fischer W. W., Schroeder S., Lacassie J. P., Beukes N. J., Goldberg T., Strauss H., Horstmann U. E., Schrag D. P. and Knoll A. H. (2009) Isotopic constraints on the Late Archean carbon cycle from the Transvaal Supergroup along the western margin of the Kaapvaal Craton, South Africa. *Precambrian Res.* **169**, 15–27.

Gill B. C., Lyons T. W. and Frank T. D. (2008) Behavior of carbonate-associated sulfate during meteoric diagenesis and implications for the sulfur isotope paleoproxy. *Geochim. Cosmochim. Acta* **72**, 4699–4711.

Gleason J. D., Gutzmer J., Kesler S. E. and Zwingmann H. (2011) 2.05-Ga Isotopic Ages for Transvaal Mississippi Valley–Type Deposits: Evidence for Large-Scale Hydrothermal Circulation around the Bushveld Igneous Complex, South Africa. *J. Geol.* **119**, 69–80.

Grotzinger J. P. and Kasting J. F. (1993) New constraints on Precambrian ocean composition. *J. Geol.* **101**, 235–243.

Guo Q., Strauss H., Kaufman A. J., Schröder S., Gutzmer J., Wing B., Baker M. A., Bekker A., Jin Q., Kim S.-T. and Farquhar J. (2009) Reconstructing Earth's surface oxidation across the Archean-Proterozoic transition. *Geology* **37**, 399–402.

Halevy I. (2013) Production, preservation, and biological processing of mass-independent sulfur isotope fractionation in the Archean surface environment. *Proc. Natl. Acad. Sci.* Available at: http://www.pnas.org/content/early/2013/04/08/1213148110.abstract.

Harman C. E., Pavlov A. A., Babikov D. and Kasting J. F. (2018) Chain formation as a mechanism for mass-independent fractionation of sulfur isotopes in the Archean atmosphere. *Earth Planet. Sci. Lett.* **496**, 238–247.

Holland H. D. (1984) *The chemical evolution of the atmosphere and oceans*., Princeton University Press.

Hulston J. R. and Thode H. G. (1965) Variations in the S33, S34, and S36 Contents of Meteorites and Their Relation to Chemical and Nuclear Effects. *J. Geophys. Res.* **70**, 3475–3484.

Izon G., Zerkle A. L., Williford K. H., Farquhar J., Poulton S. W. and Claire M. W. (2017) Biological regulation of atmospheric chemistry en route to planetary oxygenation. *Proc. Natl. Acad. Sci.* **114**, E2571.

Izon G., Zerkle A. L., Zhelezinskaia I., Farquhar J., Newton R. J., Poulton S. W., Eigenbrode J. L. and Claire M. W. (2015) Multiple oscillations in Neoarchaean atmospheric chemistry. *Earth Planet. Sci. Lett.* **431**, 264–273.

Jamieson J. W., Wing B. A., Farquhar J. and Hannington M. D. (2013) Neoarchaean seawater sulphate concentrations from sulphur isotopes in massive sulphide ore. *Nat. Geosci* **6**, 61–64.

Johnson J. E., Gerpheide A., Lamb M. P. and Fischer W. W. (2014) O2 constraints from Paleoproterozoic detrital pyrite and uraninite. *Geol. Soc. Am. Bull.* Available at: http://gsabulletin.gsapubs.org/content/early/2014/02/27/B30949.1.abstract.

Johnson J. E., Webb S. M., Condit C. B., Beukes N. J. and Fisher W. W. (2019) Effects of metamorphism and metasomatism on manganese mineralogy: Examples from the Transvaal Supergroup. *South Afr. J. Geol.* **122**.

Johnson J. E., Webb S. M., Thomas K., Ono S., Kirschvink J. L. and Fischer W. W. (2013) Manganese-oxidizing photosynthesis before the rise of cyanobacteria. *Proc. Natl. Acad. Sci.* **110**, 11238–11243.

Johnston D. T. (2011) Multiple sulfur isotopes and the evolution of Earth's surface sulfur cycle. *Earth-Sci. Rev.* **106**, 161–183.

Kamber B. S. and Whitehouse M. J. (2007) Micro-scale sulphur isotope evidence for sulphur cycling in the late Archean shallow ocean. *Geobiology* **5**, 5–17.

Kaneko Y. and Miyano T. (1990) Contact metamorphism of the Bushveld Complex in the northeastern Transvaal, South Africa. *J. Mineral. Petrol. Econ. Geol.* **85**, 66–81.

Kasting J. F. (1989) Long-term stability of the earth's climate. *Palaeogeogr. Palaeoclimatol. Palaeoecol.* **75**, 83–95.

Kaufman A. J., Johnston D. T., Farquhar J., Masterson A. L., Lyons T. W., Bates S., Anbar A. D., Arnold G. L., Garvin J. and Buick R. (2007) Late Archean Biospheric Oxygenation and Atmospheric Evolution. *Science* **317**, 1900–1903.

Knoll A. H. and Beukes N. J. (2009) Introduction: Initial investigations of a Neoarchean shelf margin-basin transition (Transvaal Supergroup, South Africa). *Precambrian Res.* **169**, 1–14.

Lowe D. R., Drabon N. and Byerly G. R. (2019) Crustal fracturing, unconformities, and barite deposition, 3.26–3.23 Ga, Barberton Greenstone Belt, South Africa. *Precambrian Res.* **327**, 34–46.

Luo G., Ono S., Beukes N. J., Wang D. T., Xie S. and Summons R. E. (2016) Rapid oxygenation of Earth's atmosphere 2.33 billion years ago. *Sci. Adv.* **2**. Available at: http://advances.sciencemag.org/content/advances/2/5/e1600134.full.pdf.

Lyons J. R. (2009) Atmospherically-derived mass-independent sulfur isotope signatures, and incorporation into sediments. *Chem. Geol.* **267**, 164–174.

Lyons J. R. (2007) Mass-independent fractionation of sulfur isotopes by isotope-selective photodissociation of SO2. *Geophys. Res. Lett.* **34**, L22811.

Lyons J. R., Herde H., Stark G., Blackie D. S., Pickering J. C. and de Oliveira N. (2018) VUV pressure-broadening in sulfur dioxide. *J. Quant. Spectrosc. Radiat. Transf.* **210**, 156–164.

Masterson A. L., Farquhar J. and Wing B. A. (2011) Sulfur mass-independent fractionation patterns in the broadband UV photolysis of sulfur dioxide: Pressure and third body effects. *Earth Planet. Sci. Lett.* **306**, 253–260.

Miyano T and Beukes N. (1997) Mineralogy and petrology of the contact metamorphosed amphibole asbestos-bearing Penge iron formation, Eastern Transvaal, South Africa. *J. Petrol.* **38**, 651–676.

Miyano T. and Beukes N. J. (1997) Mineralogy and Petrology of the Contact Metamorphosed Amphibole Asbestos-bearing Penge Iron Formation, Eastern Transvaal, South Africa. *J. Petrol.* **38**, 651–676.

Miyano T. and Beukes N. J. (1984) Phase relations of stilpnomelane, ferri-annite, and riebeckite in very low-grade metamorphosed iron-formations. *South Afr. J. Geol.* **87**, 111–124.

Muller É., Philippot P., Rollion-Bard C. and Cartigny P. (2016) Multiple sulfur-isotope signatures in Archean sulfates and their implications for the chemistry and dynamics of the early atmosphere. *Proc. Natl. Acad. Sci.* **113**, 7432–7437.

Ono S., Beukes N. J. and Rumble D. (2009a) Origin of two distinct multiple-sulfur isotope compositions of pyrite in the 2.5 Ga Klein Naute Formation, Griqualand West Basin, South Africa. *Precambrian Res.* **169**, 48–57.

Ono S., Eigenbrode J. L., Pavlov A. A., Kharecha P., Rumble Iii D., Kasting J. F. and Freeman K. H. (2003) New insights into Archean sulfur cycle from mass-independent sulfur isotope records from the Hamersley Basin, Australia. *Earth Planet. Sci. Lett.* **213**, 15–30.

Ono S., Kaufman A. J., Farquhar J., Sumner D. Y. and Beukes N. J. (2009b) Lithofacies control on multiple-sulfur isotope records and Neoarchean sulfur cycles. *Precambrian Res.* **169**, 58–67.

Ono S., Whitehill A. R. and Lyons J. R. (2013) Contribution of isotopologue self-shielding to sulfur mass-independent fractionation during sulfur dioxide photolysis. *J. Geophys. Res. Atmospheres* **118**, 2444–2454.

Ono S., Wing B., Johnston D., Farquhar J. and Rumble D. (2006) Mass-dependent fractionation of quadruple stable sulfur isotope system as a new tracer of sulfur biogeochemical cycles. *Geochim. Cosmochim. Acta* **70**, 2238–2252.

Paris G., Adkins J. F., Sessions A. L., Webb S. M. and Fischer W. W. (2014) Neoarchean carbonate–associated sulfate records positive Δ33S anomalies. *Science* **346**, 739–741.

Paris G., Sessions A. L., Subhas A. V. and Adkins J. F. (2013) MC-ICP-MS measurement of δ34S and Δ33S in small amounts of dissolved sulfate. *Chem. Geol.* **345**, 50–61.

Pavlov A. A. and Kasting J. F. (2002) Mass-Independent Fractionation of Sulfur Isotopes in Archean Sediments: Strong Evidence for an Anoxic Archean Atmosphere. *Astrobiology* **2**, 27–41.

Philippot P., Ávila J. N., Killingsworth B. A., Tessalina S., Baton F., Caquineau T., Muller E., Pecoits E., Cartigny P., Lalonde S. V., Ireland T. R., Thomazo C., van Kranendonk M. J. and Busigny V. (2018) Globally asynchronous sulphur isotope signals require re-definition of the Great Oxidation Event. *Nat. Commun.* **9**, 2245.

Philippot P., Van Zuilen M., Lepot K., Thomazo C., Farquhar J. and Van Kranendonk M. J. (2007) Early Archaean Microorganisms Preferred Elemental Sulfur, Not Sulfate. *Science* **317**, 1534.

Philippot P., van Zuilen M. and Rollion-Bard C. (2012) Variations in atmospheric sulphur chemistry on early Earth linked to volcanic activity. *Nat. Geosci* **5**, 668–674.

Present T. M., Gutierrez M., Paris G., Kerans C., Grotzinger J. P. and Adkins J. F. (2019) Diagenetic controls on the isotopic composition of carbonate-associated sulphate in the Permian Capitan Reef Complex, West Texas. *Sedimentology* **0**. Available at: https://doi.org/10.1111/sed.12615 [Accessed August 27, 2019].

Present T. M., Paris G., Burke A., Fischer W. W. and Adkins J. F. (2015) Large Carbonate Associated Sulfate isotopic variability between brachiopods, micrite, and other sedimentary components in Late Ordovician strata. *Earth Planet. Sci. Lett.* **432**, 187–198.

Raven M. R., Adkins J. F., Werne J. P., Lyons T. W. and Sessions A. L. (2015) Sulfur isotopic composition of individual organic compounds from Cariaco Basin sediments. *Org. Geochem.* **80**, 53–59.

Rennie V. C. F., Paris G., Sessions A. L., Abramovich S. and Turchyn A. V. (2014) Foraminiferal calcite provides new insight into the coupled carbon & sulfur isotope evolution of the ocean in the Palaeogene. In Agouron Symposium.

Rennie V. C. F., Paris G., Sessions A. L., Abramovich S., Turchyn A. V. and Adkins J. F. (2018) Cenozoic record of δ34S in foraminiferal calcite implies an early Eocene shift to deep-ocean sulfide burial. *Nat. Geosci.* Available at: https://doi.org/10.1038/s41561-018-0200-y.

Richardson J. A., Newville M., Lanzirotti A., Webb S. M., Rose C. V., Catalano J. G. and Fike D. A. (2019a) Depositional and diagenetic constraints on the abundance and spatial variability of carbonate-associated sulfate. *Chem. Geol.* **523**, 59–72.

Richardson J. A., Newville M., Lanzirotti A., Webb S. M., Rose C. V., Catalano J. G. and Fike D. A. (2019b) The source of sulfate in brachiopod calcite: Insights from μ-XRF imaging and XANES spectroscopy. *Chem. Geol.* **529**, 119328.

Rickard D. T. (1975) Kinetics and mechanism of pyrite formation at low temperatures. *Am. J. Sci.* **275**, 636–652.

Roerdink D. L., Mason P. R. D., Farquhar J. and Reimer T. (2012) Multiple sulfur isotopes in Paleoarchean barites identify an important role for microbial sulfate reduction in the early marine environment. *Earth Planet. Sci. Lett.* **331–332**, 177–186.

Roerdink D. L., Mason P. R. D., Whitehouse M. J. and Reimer T. (2013) High-resolution quadruple sulfur isotope analyses of 3.2 Ga pyrite from the Barberton Greenstone Belt in South Africa reveal distinct environmental controls on sulfide isotopic arrays. *Geochim. Cosmochim. Acta* **117**, 203–215.

Sagan C. and Chyba C. (1997) The Early Faint Sun Paradox: Organic Shielding of Ultraviolet-Labile Greenhouse Gases. *Science* **276**, 1217.

Sagan C. and Mullen G. (1972) Earth and Mars: Evolution of Atmospheres and Surface Temperatures. *Science* **177**, 52.

Savarino J., Romero A., Cole-Dai J., Bekki S. and Thiemens M. H. (2003) UV induced mass-independent sulfur isotope fractionation in stratospheric volcanic sulfate. *Geophys. Res. Lett.* **30**, 2131.

Schiffries C. M. and Skinner B. J. (1987) The Bushveld hydrothermal system; field and petrologic evidence. *Am. J. Sci.* **287**, 566–595.

Shen Y., Buick R. and Canfield D. E. (2001) Isotopic evidence for microbial sulphate reduction in the early Archaean era. *Nature* **410**, 77–81.

Shen Y., Farquhar J., Masterson A., Kaufman A. J. and Buick R. (2009) Evaluating the role of microbial sulfate reduction in the early Archean using quadruple isotope systematics. *Earth Planet. Sci. Lett.* **279**, 383–391.

Stüeken E. E., Catling D. C. and Buick R. (2012) Contributions to late Archaean sulphur cycling by life on land. *Nat. Geosci.* **5**, 722.

Sumner D. Y. (1997a) Carbonate precipitation and oxygen stratification in late Archean seawater as deduced from facies and stratigraphy of the Gamohaan and Frisco formations, Transvaal Supergroup, South Africa. *Am. J. Sci.* **297**, 455–487.

Sumner D. Y. (1997b) Late Archean calcite-microbe interactions; two morphologically distinct microbial communities that affected calcite nucleation differently. *Palaios* **12**, 302–318.

Sumner D. Y. (2002) *Neoarchean carbonates – clues to early life and early ocean chemistry.*,

Sumner D. Y. and Beukes N. J. (2006) Sequence Stratigraphic Development of the Neoarchean Transvaal carbonate platform, Kaapvaal Craton, South Africa. *South Afr. J. Geol.* **109**, 11–22.

Sumner D. Y. and Bowring S. A. (1996) U-Pb geochronologic constraints on deposition of the Campbellrand Subgroup, Transvaal Supergroup, South Africa. *Precambrian Res.* **79**, 25–35.

Sumner D. Y. and Grotzinger J. P. (1996) Herringbone calcite; petrography and environmental significance. *J. Sediment. Res.* **66**, 419–429.

Sumner D. Y. and Grotzinger J. P. (2004) Implications for Neoarchaean ocean chemistry from primary carbonate mineralogy of the Campbellrand-Malmani Platform, South Africa. *Sedimentology* **51**, 1273–1299.

Thomazo C., Ader M., Farquhar J. and Philippot P. (2009) Methanotrophs regulated atmospheric sulfur isotope anomalies during the Mesoarchean (Tumbiana Formation, Western Australia). *Earth Planet. Sci. Lett.* **279**, 65–75.

Torres M. A., Paris G., Adkins J. F. and Fischer W. W. (2018) Riverine evidence for isotopic mass balance in the Earth's early sulfur cycle. *Nat. Geosci.* Available at: https://doi.org/10.1038/s41561-018-0184-7.

Toyama K., Paytan A., Sawada K. and Hasegawa T. (2020) Sulfur isotope ratios in co-occurring barite and carbonate from Eocene sediments: A comparison study. *Chem. Geol.* **535**, 119454.

Truswell J. F. and Eriksson K. A. (1973) Stromatolitic associations and their palaeo-environmental significance: A re-appraisal of a lower Proterozoic locality from the northern Cape Province, SouthAfrica. *Sediment. Geol.* **10**, 1–23.

Ueno Y., Johnson M. S., Danielache S. O., Eskebjerg C., Pandey A. and Yoshida N. (2009) Geological sulfur isotopes indicate elevated OCS in the Archean atmosphere, solving faint young sun paradox. *Proc. Natl. Acad. Sci. U. S. A.* **106**, 14784–14789.

Ueno Y., Ono S., Rumble D. and Maruyama S. (2008) Quadruple sulfur isotope analysis of ca. 3.5 Ga Dresser Formation: New evidence for microbial sulfate reduction in the early Archean. *Geochim. Cosmochim. Acta* **72**, 5675–5691.

Van Kranendonk M. J. (2006) Volcanic degassing, hydrothermal circulation and the flourishing of early life on Earth: A review of the evidence from c. 3490-3240 Ma rocks of the Pilbara Supergroup, Pilbara Craton, Western Australia. *Earth-Sci. Rev.* **74**, 197–240.

Walraven F., Armstrong R. A. and Kruger F. J. (1990) A chronostratigraphic framework for the north-central Kaapvaal craton, the Bushveld Complex and the Vredefort structure. *Tectonophysics* **171**, 23–48.

Webb S. M. (2005) SIXPack a Graphical User Interface for XAS Analysis Using IFEFFIT. *Phys. Scr.*, 1011.

Whitehill A. R., Jiang B., Guo H. and Ono S. (2015) SO2 photolysis as a source for sulfur mass-independent isotope signatures in stratospehric aerosols. *Atmos Chem Phys* **15**, 1843–1864.

Whitehill A. R. and Ono S. (2012) Excitation band dependence of sulfur isotope mass-independent fractionation during photochemistry of sulfur dioxide using broadband light sources. *Geochim. Cosmochim. Acta* **94**, 238–253.

Whitehill A. R., Xie C., Hu X., Xie D., Guo H. and Ono S. (2013) Vibronic origin of sulfur mass-independent isotope effect in photoexcitation of SO2 and the implications to the early earth's atmosphere. *Proc. Natl. Acad. Sci.* Available at: http://www.pnas.org/content/early/2013/07/05/1306979110.abstract.

Wotte T., Shields-Zhou G. A. and Strauss H. (2012) Carbonate-associated sulfate: Experimental comparisons of common extraction methods and recommendations toward a standard analytical protocol. *Chem. Geol.* **326–327**, 132–144.

Zahnle K., Claire M. W. and Catling (2006) The loss of mass-independent fractionation in sulfur due to a Palaeoproterozoic collapse of atmospheric methane. *Geobiology* **4**, 271–283.

Zerkle A. L., Claire M. W., Domagal-Goldman S. D., Farquhar J. and Poulton S. W. (2012) A bistable organic-rich atmosphere on the Neoarchaean Earth. *Nat. Geosci* **5**, 359–363.

Zhelezinskaia I., Kaufman A. J., Farquhar J. and Cliff J. (2014) Large sulfur isotope fractionations associated with Neoarchean microbial sulfate reduction. *Science* **346**, 742–744.

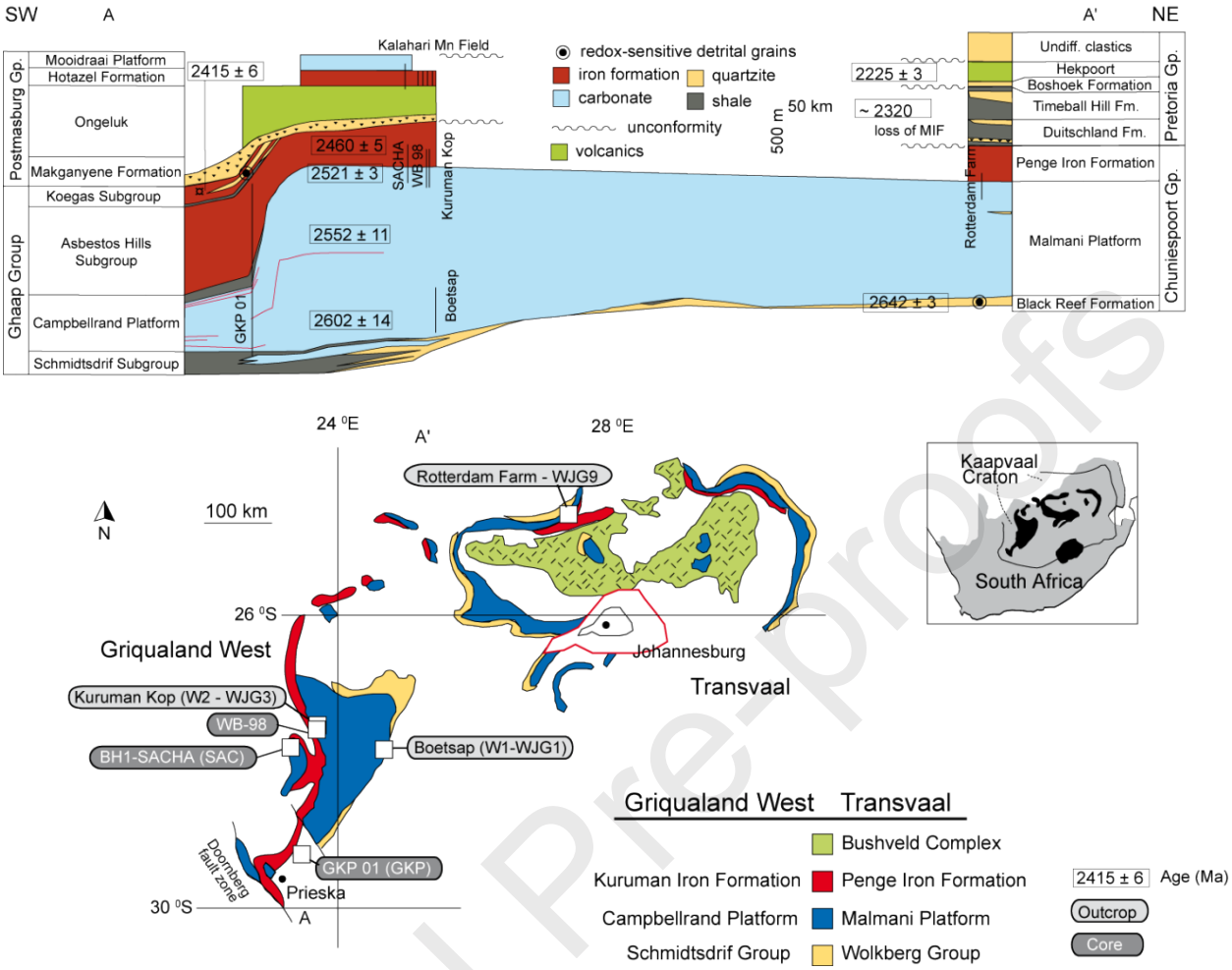

Figure 1 Structural cross-section through the Campbellrand platform (top) and geologic map (bottom) of the Kaapvaal Craton showing the cross-section transect through the surface exposures of the Late Archean Transvaal Supergroup, and the two structural sub-basins, Griqualand West and Transvaal. Stratigraphic sections and sample locations for this study are shown. Modified from (Sumner and Beukes, 2006; Johnson et al., 2013; Johnson et al., 2014). For each location we indicated in parentheses the code used for the sample names, when different from the core/location names. All samples were collected for the current study except W1 and W2, which are samples previously analyzed (Paris et al., 2014).

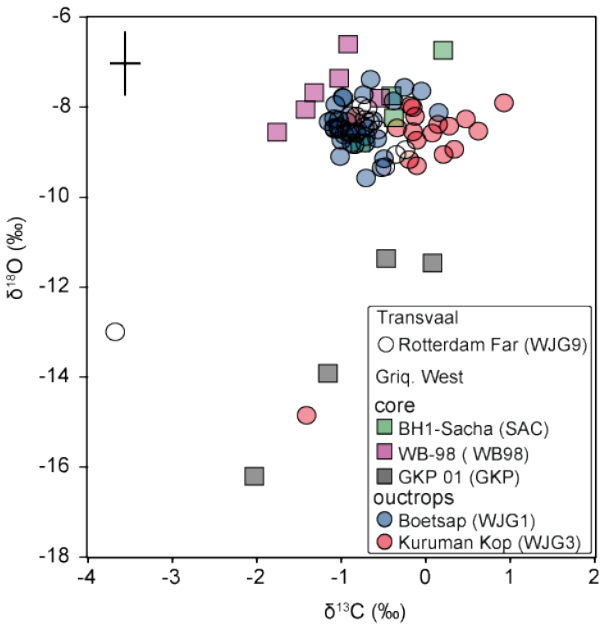

Figure 2 $\delta^{13}C$ and $\delta^{18}O$ data of carbonate in samples that were also analyzed for sulfur isotopes. The symbols represent the various collection locations with squares indicating cores, circles indicating outcrops, open symbols are for samples from the Transvaal area and filled symbols are for samples for Griqualand West. 2SD is 0.25‰ for $\delta^{13}C$ and 0.85‰ for $\delta^{18}O$.

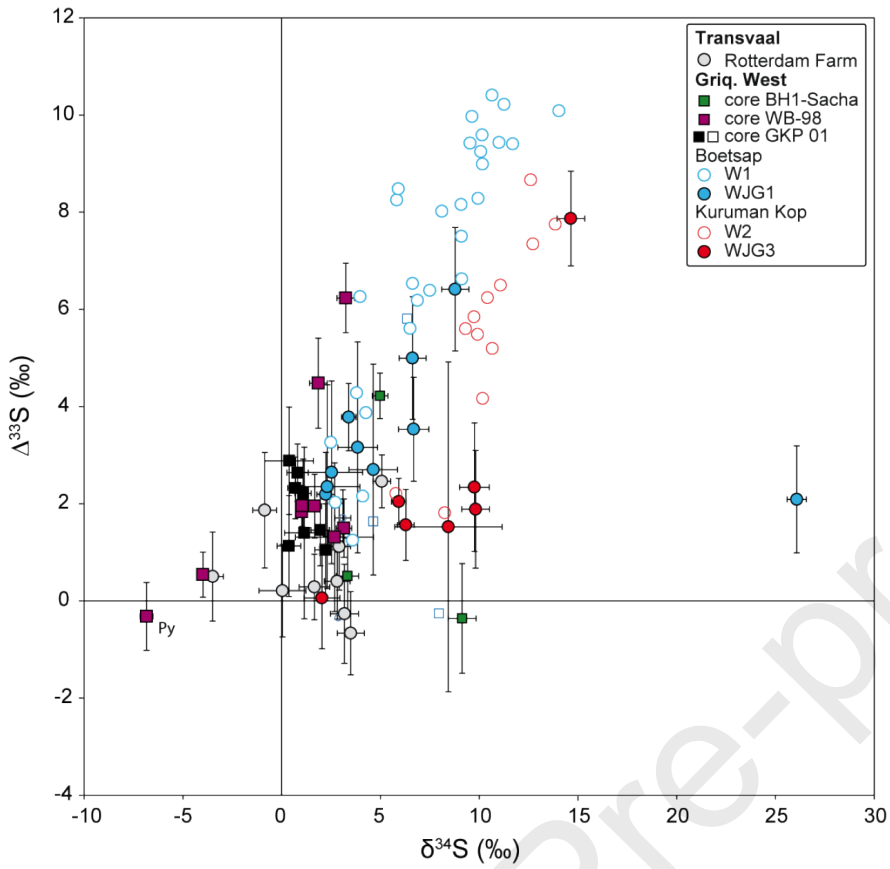

Figure 3 Cross-plots of $\Delta^{33}S$ vs. $\delta^{34}S$ values. The symbols represent the various collection locations with squares indicating cores, circles indicating outcrops, open symbols are for previous data (Paris et al., 2014) and filled symbols are for new data.) Errors are plotted as 2sd.

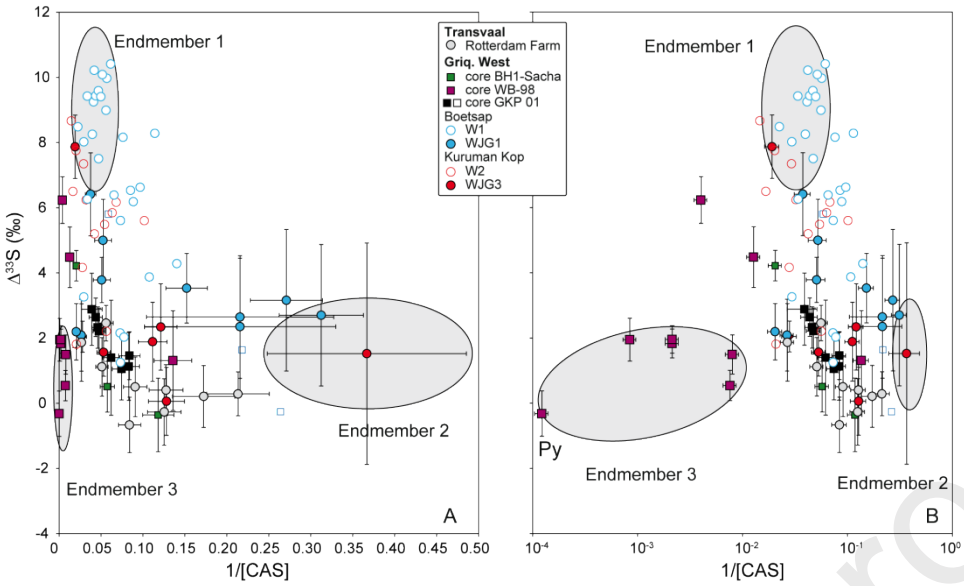

Figure 4 Cross-plots showing 1/[CAS] (g of carbonate/µg of sulfate) vs. $\Delta^{33}S$ with linear (A) or logarithmic x-axis (B). The "Py" arrow in Fig. 4 points to a sample that was drilled over a pyrite nodule and contained the highest sulfate content (>8000 ppm), the lowest $\delta^{34}S$, and a negative $\Delta^{33}S$ value. Panel B shows the most enriched data points that correspond to the samples drilled over pyrite (Py). The symbols represent the various collection locations with squares indicating cores, circles indicated outcrops, open symbols are for previously published values (Paris et al., 2014). Errors are plotted as 2sd.

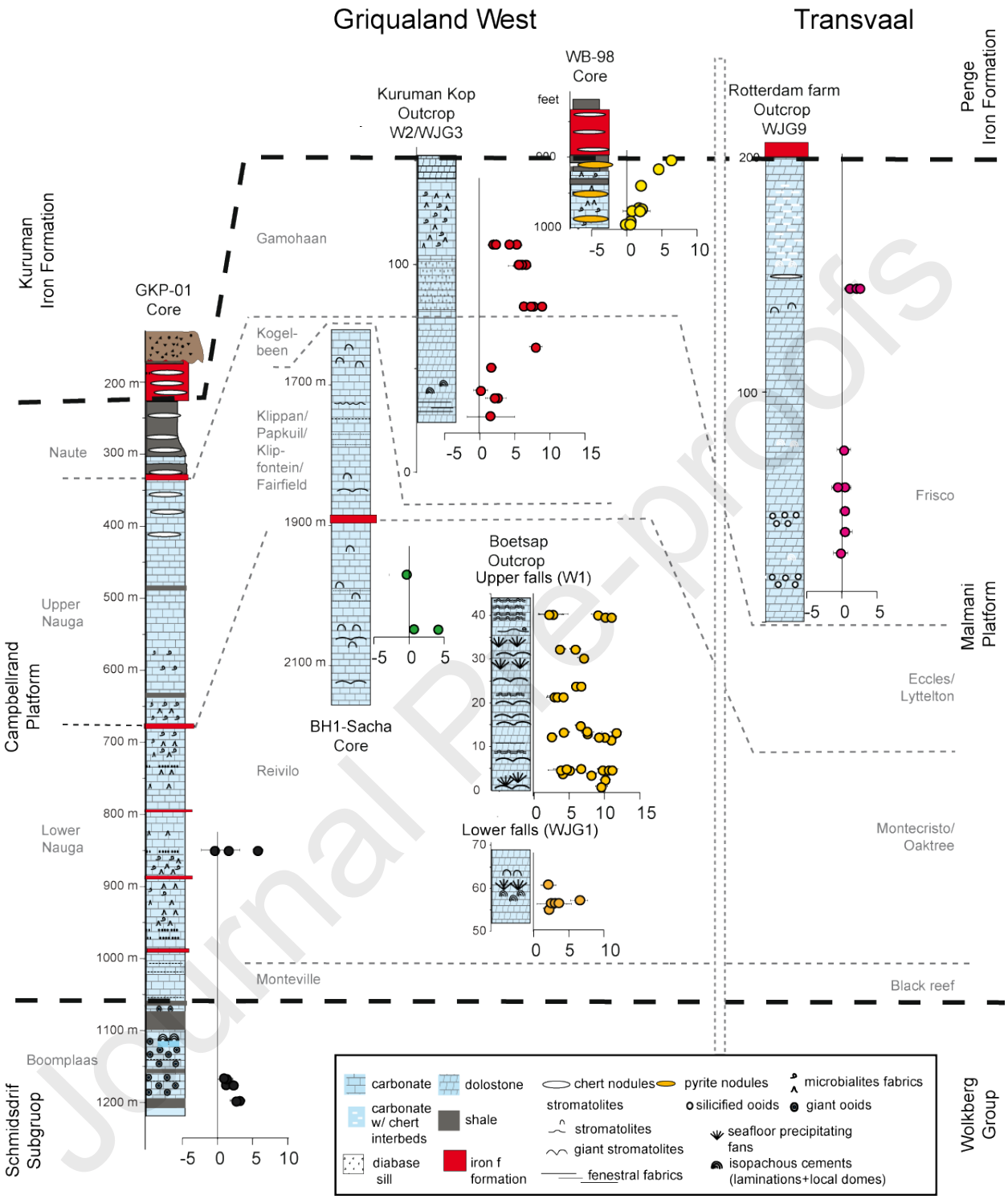

Figure 5 Stratigraphic sections of the outcrops and cores across the Campbellrand-Malmani platform showing the $\Delta^{33}S$ values. The sections are shown relative to an arbitrary datum at the

base of the platform, and otherwise correlated on sequence stratigraphic data (Sumner and Beukes, 2006).

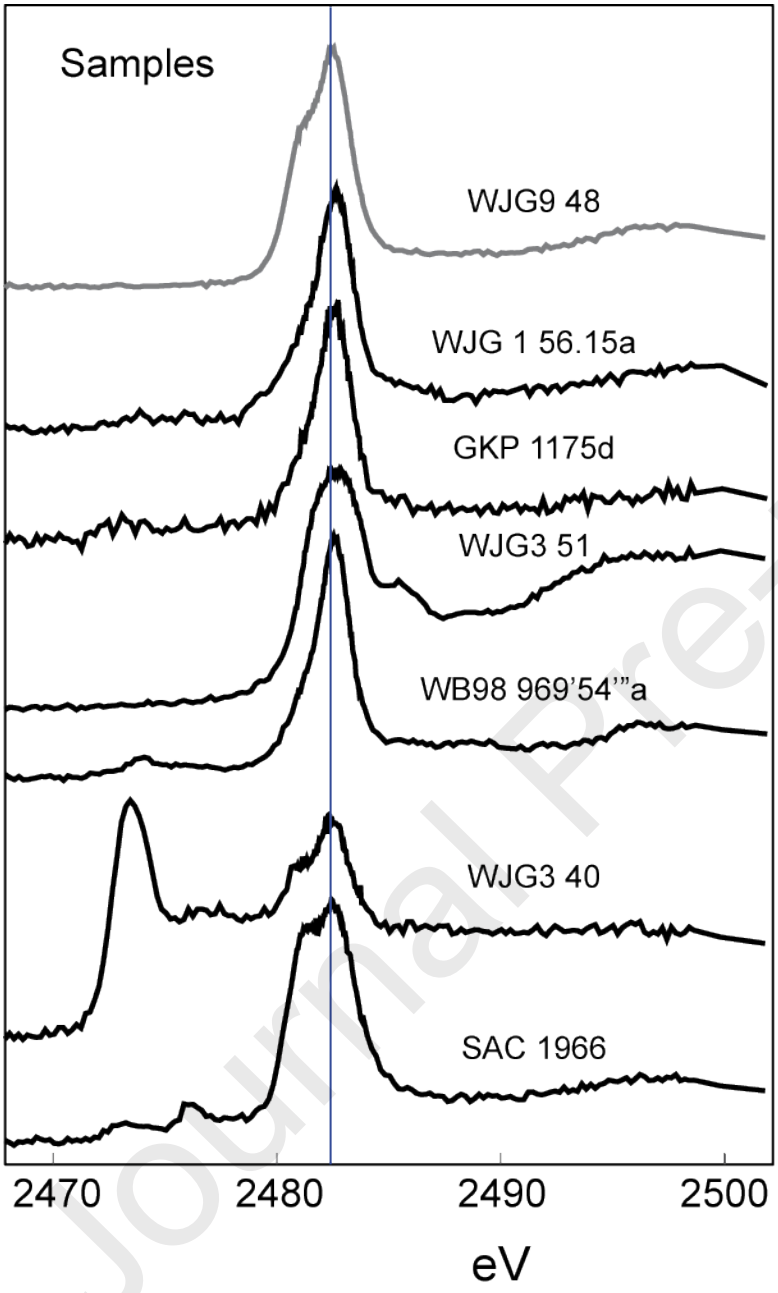

Figure 6 Sulfur K-edge XANES spectra of carbonate samples. The vertical line indicates the location of the sulfate peak.

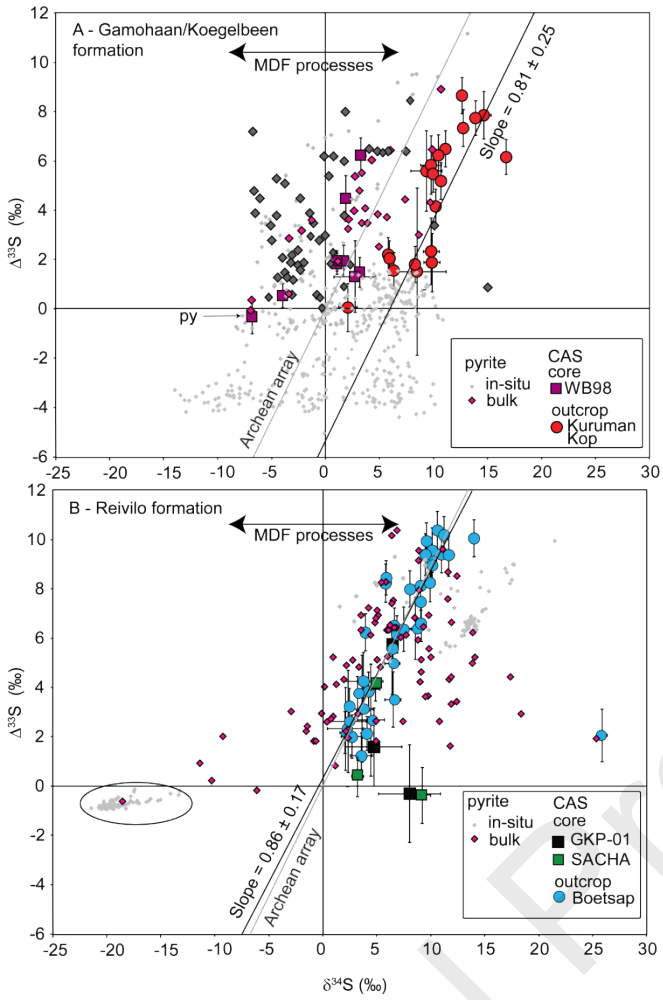

Fig. 7 Cross-plots showing $\Delta^{33}S$ vs. $\delta^{34}S$ values for the top (Gamohaan-Koegelbeen formation, A) and base of the platform (Reivilo formation, B) both from this study and from Paris et al. (2014). Thin gray lines indicate the Archean array (Ono et al., 2003; Ono et al., 2009b). In panel A, pyrite data are a compilation of the Gamohaan-Koegelbeen formations, bulk (Kaufman et al., 2007; Izon et al., 2015) and "*in-situ"* (Kamber and Whitehouse, 2007) and the Klein Naute -upper part of the Upper Nauga formations, bulk (Ono et al., 2009a; Ono et al., 2009b) and "*in-situ*" (Ono et al., 2009a; Fischer et al., 2014). The arrow at lower left indicates the point drilled through a pyrite nodule. The thick line indicates the linear regression calculated from the data. In panel B, pyrite data are a compilation of data for the Reivilo formation, bulk (Farquhar et al., 2013; Izon et al., 2015; Ono et al., 2009b; Zerkle et al., 2012) and "*in-situ*" (Farquhar et al., 2013). The thick lines indicate the linear regression calculated from the data, excluding the data point at $\delta^{34}S$=25 ‰. The ellipse indicates the pyrite data with negative $\Delta^{33}S$ values.

samples	CAS	SO4-ester	gypsum	barite	sulfonate	sulfoxide	pyrite	S8	kerogen type 1	kerogen type 2	methionine
GKP 1175 d	29	12	28	_	2	_	3	3	13	6	4
WJG3 40	7	9	_	2	1	10	10	12	6	21	21
SAC 1966	34	27	_	9	15.0	3	_	_	6	6	_
WJG1 56.15a	43	27	_	8	8	_	_	_	7	5	_
WJG9 48a	33	27	_	11	14	_	_	_	8	4	_
WB98 969'54''a	48	26	_	5	_	_	_	_	10	7	2
WJG3 51	_	_		_		_	no fit	_	_	_	_

Table 1 Relative proportions of sulfur species determined from XANES spectra

Appendix: data repository

Supplementary information (Figs. S1 to S6)